Rare-earth-doped ceria nanostructures for oxidation of soot with different reactivities: Role of catalyst restructuring and surface acidity in soot-catalyst contact renewal

Original

Rare-earth-doped ceria nanostructures for oxidation of soot with different reactivities: Role of catalyst restructuring and surface acidity in soot-catalyst contact renewal / Sartoretti, Enrico; Hagen, Fabian P.; Novara, Chiara; Piumetti, Marco; Bockhorn, Henning; Trimis, Dimosthenis; Bensaid, Samir. - In: JOURNAL OF ENVIRONMENTAL CHEMICAL ENGINEERING. - ISSN 2213-3437. - ELETTRONICO. - 14:3(2026), pp. 1-14. [10.1016/j.jece.2026.123057]

Publisher:
Elsevier

Published
DOI:10.1016/j.jece.2026.123057

Journal of Environmental Chemical Engineering 14 (2026) 123057

Contents lists available at ScienceDirect

Journal of Environmental Chemical Engineering

journal homepage: www.elsevier.com/locate/jece

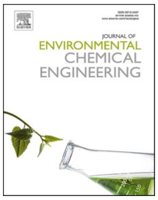

Rare-earth-doped ceria nanostructures for oxidation of soot with different reactivities: Role of catalyst restructuring and surface acidity in soot-catalyst contact renewal

Enrico Sartoretti [a,1,*], Fabian P. Hagen [b,1], Chiara Novara [a], Marco Piumetti [a], Henning Bockhorn [b], Dimosthenis Trimis [b], Samir Bensaid [a]

[a] *Department of Applied Science and Technology, Politecnico di Torino, Corso Duca degli Abruzzi, 24, Turin 10129, Italy*
[b] *Engler-Bunte-Institute, Combustion Technology, Karlsruhe Institute of Technology (KIT), Karlsruhe, Engler-Bunte-Ring 7, Karlsruhe 76131, Germany*

ARTICLE INFO

Keywords:
Doped ceria
Nanocatalysts
Soot oxidation
Acid sites
Soot-catalyst contact
Restructuring

ABSTRACT

Catalytic soot oxidation is a key process for particulate filter regeneration, yet catalyst performance is often evaluated using a single soot type, overlooking the strong influence of soot physicochemical properties on oxidation behavior. In this work, the impact of intrinsic soot reactivity on catalytic oxidation was systematically investigated using soot samples with distinct structural, textural, and chemical characteristics. Model flame soots and commercial carbon blacks with different initial reactivity were oxidized over three ceria-based nanostructured catalysts, i.e. pure ceria, equimolar ceria–praseodymia, and equimolar ceria-lanthana. Catalytic activity was assessed under loose and tight contact conditions by temperature-programmed oxidation, complemented by kinetic analysis and stepwise oxidation experiments combined with high-resolution transmission electron microscopy. Regardless of the catalyst, soot reactivity was primarily governed by nanostructural order, as reflected by fringe length, primary particle size, and C/H ratio. Rare earth-doped ceria catalysts exhibited enhanced activity compared to pure ceria, with ceria-lanthana showing the lowest oxidation temperatures in all conditions and the smallest sensitivity to contact degree. This behavior mainly arises from its higher surface acidity, combined with highly abundant surface oxygen species, improved oxygen storage and release capacity, and morphology-induced contact enhancement. HRTEM observations revealed that Ce50La50 dynamically restructures during oxidation, continuously generating new soot-catalyst contact sites that sustain activity under limited-contact conditions. These results highlight the critical interplay between soot properties, catalyst surface chemistry and contact dynamics, thus providing guidance for the rational design of soot oxidation catalysts combining high activity with robustness under operating conditions.

1. Introduction

Particulate matter generated as a byproduct of hydrocarbon combustion poses significant threats to both human health and the environment. Its fine particles, especially those with diameters below 2.5 µm, are linked to severe cardiovascular and respiratory diseases, such as stroke or lung cancer [1,2], and can contribute to climate change through effects like altering albedo and affecting cloud formation [3]. To mitigate these harmful emissions, exhaust after-treatment systems, and especially particulate filters (such as diesel and gasoline particulate filters), have been widely adopted as effective technologies for capturing and removing soot particles [4,5]. These filters rely on periodic regeneration through soot oxidation, which requires temperatures above 600 °C and is hence a fuel-consuming process. Nevertheless, the use of proper catalysts to promote soot oxidation can make regeneration less energy-intensive [6].

The catalytic oxidation of soot is a complex gas-solid-solid reaction, in which the physical contact between soot particles and catalyst is a crucial factor influencing overall performance [7,8]. Although the total specific surface area of the catalyst is relevant, the accessibility of active sites is far more critical [9,10]. Since catalyst morphology plays a pivotal role in promoting effective contact, materials with various structures

---

* Corresponding author.
E-mail address: enrico.sartoretti@polito.it (E. Sartoretti).
[1] These authors equally contributed to this work

https://doi.org/10.1016/j.jece.2026.123057
Received 6 February 2026; Received in revised form 10 April 2026; Accepted 6 May 2026

have been engineered to optimize solid-solid interactions. For instance, three-dimensionally ordered macroporous (3DOM) catalysts with large and uniform pores (>50 nm) allow soot particles to penetrate the catalyst structure, thereby enhancing contact efficiency [11,12]. Other tailored morphologies, such as mesoporous structures, hollow frameworks, nanoflower-like particles, and fibrous catalysts, have also been explored to improve contact and active site accessibility [13–16]. Additionally, catalysts with low melting points, particularly those containing alkali metals, can exhibit enhanced mobility of surface atoms at high temperature, leading to improved contact between the catalyst and soot particles, which is especially beneficial in poor contact conditions [17,18]. In the last years, Mei at al. proposed an electrification strategy for low temperature soot oxidation using conductive oxide catalysts, reporting that electrostatic interactions between catalyst and soot account for enhanced contact efficiency [19,20].

Multiple interconnected mechanisms are involved in catalytic soot oxidation, primarily linked to the generation and transfer of active oxygen species [21–24]. Effective catalysts are able to produce highly reactive species at their surface, such as superoxide (O_2^-) and peroxide (O_2^{2-}) ions, which can migrate towards soot particles via spillover. In case of metal oxides with multiple ion valency states, the Mars-van Krevelen-like (MvK) mechanism can also occur in parallel [21,25]. This redox pathway involves two key steps: first, soot is directly oxidized by lattice oxygen from the catalyst, creating a region enriched with oxygen vacancies and reduced cations at the soot-catalyst interface; the catalyst surface is subsequently reoxidized by gaseous O_2, with oxygen vacancy replenishment possibly leading to the generation of additional active oxygen species [26]. Oxygen vacancies can indeed serve as active sites, enhancing both oxygen mobility and activation [27].

Various catalyst formulations have been studied for their ability to promote these mechanisms, including noble metals (e.g., Ag, Pt [28–31]), transition metal oxides (e.g., Co, Mn, Cu, Cr, Fe [7,14, 32–35]), rare earth oxides (e.g., Ce, Pr, La [36–39]), and alkali metals (e.g., K, Na [17,26,40]). Among them, CeO_2 is a particularly important redox oxide, commonly employed due to its excellent oxygen storage and release capabilities [36,41]. The morphology of ceria-based materials can be tuned to produce nanoparticles with different exposed crystal facets, each exhibiting distinct reactivity and soot-contact characteristics [42,43]. Furthermore, doping ceria with other cations can significantly enhance lattice oxygen mobility, thereby fostering the catalyst redox cycle and the MvK mechanism [37]. However, most catalytic studies evaluate activity only against a single soot sample with a defined reactivity, rather than systematically exploring how soot morphology and structural properties influence catalyst performance.

Actually, the soot oxidation process is also influenced by the physicochemical properties of soot, including its nanostructure, degree of graphitization, and functional groups [44–47], which undergo continuous transformation during catalytic oxidation [48,49]. A particle nanostructure characterized by small-sized fringes under TEM observation is associated with high reactivity, whereas extended and more ordered fringes are linked to lower reactivity [45–47].The outer shells of soot particles are typically involved in the initial stages of catalytic combustion, with possible formation and consumption of oxygen-containing functional groups on the soot surface [50,51]. Oxygen adsorbed in the early stages can accelerate soot depletion later. However, after oxidation of the soot surface in close proximity to the catalyst, weakened contact can lead to reduced reaction rate or even to non-catalytic oxidation of part of the residual soot [52]. Understanding the structural evolution of catalyst and soot particles during oxidation and the mechanisms leading to the formation of new contact sites is hence crucial for the design of durable and efficient catalysts.

In contrast to most previous catalytic studies that focused on a single soot sample with fixed reactivity, the present work explicitly addresses the impact of initial soot reactivity on catalytic performance. To this end, we investigated the catalytic oxidation of various soot samples, characterized by distinct structural properties and reactivity, using three ceria-based nanostructured materials. Pure ceria was selected as a reference material, while equimolar ceria-praseodymia (Ce50Pr50) was chosen as a well-established system for soot oxidation, known for its enhanced redox properties [37,41,53–56]. Finally, equimolar ceria-lanthana (Ce50La50) was included as a promising candidate for improved performance [38,57]. The soot samples and the catalysts were thoroughly investigated, and the soot oxidation performance was assessed at different degrees of solid-solid contact. Consecutive stepwise oxidation, tracked by high-resolution transmission electron microscopy (HRTEM), enabled direct observation of the evolving catalyst-soot contact sites and provided insights into nanoparticle restructuring mechanisms.

2. Materials and methods

2.1. Synthesis of the catalysts and soot particle systems

Pure ceria (CeO_2), equimolar ceria-praseodymia (Ce50Pr50), and equimolar ceria-lanthana (Ce50La50) were prepared through a hydrothermal synthesis procedure described elsewhere [38]. $Ce(NO_3)_3{\cdot}6\,H_2O$ (99.99%), $Pr(NO_3)_2{\cdot}6\,H_2O$ (99.9%), and $La(NO_3)_3{\cdot}6\,H_2O$ (99.99%), provided by Sigma-Aldrich, were employed as metal precursors. Briefly, 20 mmol of nitrates in appropriate relative amounts were dissolved in deionized water. This first solution was added dropwise to a second solution containing 48 g of NaOH (98%, Sigma-Aldrich) in 70 mL of deionized water. After stirring at room temperature (RT) for 1 h, the mixture was aged at 180 °C for 24 h in a steel autoclave. The thus obtained slurry was rinsed with ethanol and deionized water several times to remove Na traces, dried at 70 °C, and finally calcined in air at 650 °C for 4 h.

In this work, five different soot particle systems were investigated. They were deliberately selected to span a broad range of reactivity. To this end, both model flame soot (MFS) and commercial carbon blacks (CB) were included. MFS-C_2H_2 was produced in a low-pressure (200 mbar) flat premixed laminar acetylene/oxygen flame with equivalence ratio of 2.7 and collected on quartz fiber filters. A portion of sampled MFS-C_2H_2 was subjected to Soxhlet extraction with dichloromethane (DCM) to remove soluble organic compounds, ensuring that only the insoluble carbonaceous fraction was analyzed. MFS-$T10_{3bar}$ was synthesized in a premixed elevated-pressure (3 bar) flame of a prevaporized fuel mixture containing 10 vol% toluene in iso-octane with O_2/Ar on a McKenna burner. The premixed fuel–oxidizer mixture at an equivalence ratio of 2.3 was preheated to 150 °C. The soot was collected downstream on filters. For the CB samples, three grades from Orion Engineered Carbons were used: CB-S170 (Color Black S170, gas black method), CB-SB250 (Special Black 250, furnace black process), and CB-P90 (Printex®90, furnace black process).

2.2. Catalyst and soot characterization

Powder X-ray diffraction (XRD) was performed in a Philips X'Pert PW3040 diffractometer, using Cu Kα radiation ($\lambda = 1.5418 \times 10^{-10}$ m). XRD patterns were compared with reference data from the International Centre for Diffraction Data (ICDD) database. The diffraction profiles were analyzed by means of HighScore Plus software, and peak deconvolution was performed using pseudo-Voigt functions. The average crystallite size was estimated through the Scherrer's equation, while the unit cell size was calculated using the Nelson-Riley function. Instrumental peak broadening was corrected using a LaB_6 calibration standard.

The specific surface area (SSA) of the catalysts was measured through nitrogen physisorption at −196 °C in a Micromeritics Tristar II 3020, using the Brunauer–Emmett–Teller (BET) method in the 0.1 – 0.3 range of relative pressure (p/p°). The total pore volume (V_p) was determined from the quantity of nitrogen adsorbed at p/p° of 0.98. The average pore diameter (D_p) was estimated by applying the Barrett-

Joyner-Halenda (BJH) method to the desorption branch. A pretreatment at 200 °C for 2 h in N_2 flow was carried out prior to the analysis. The SSA of the soot samples was measured using a BELSORP-mini analyzer (BEL Japan Inc.) with nitrogen physisorption at −196 °C. The instrument was calibrated with internal standards, and samples were degassed under vacuum at 105 °C before analysis.

The C/H ratio of the soot samples was determined by elemental analysis using a Vario Micro Cube analyzer (Elementar Analysensysteme GmbH). Carbon, hydrogen, and nitrogen contents were quantified with thermoconductivity (TCD) and infrared (IR) detectors. Approximately 2.5 mg of soot were analyzed, and carbon and hydrogen mass fractions were converted into molar percentages to calculate the atomic C/H ratio.

Raman spectra of the samples were recorded using a Renishaw InVia Raman microscope with a 514.5 nm excitation wavelength and a 5x objective. Three spectra with an acquisition time of 225 s were collected in different regions and averaged. Spectral deconvolution (performed according to the procedure reported in [58]) allowed to calculate the D/F_{2g} ratio between the areas of the defect band and the main F_{2g} peak of ceria, indicative of defect abundance.

The morphology of the three catalysts was studied using a Zeiss Merlin field emission scanning electron microscope (FESEM), equipped with an Oxford X-Act detector for energy dispersive X-ray spectroscopy. Prior to the analysis, the powder was coated with a 5-nm-thick Pt layer via sputter deposition.

The primary particle sizes and the size distributions of the fringes embedded in soot particles were determined by high-resolution transmission electron microscopy (HRTEM). Soot samples were dispersed in ultrapure water using ultrasonication and deposited onto carbon-coated copper grids. HRTEM images were acquired with a Philips CM200 microscope (ThermoFisher Scientific Inc.) operated at 200 kV. Primary particle size distributions were obtained from HRTEM images using an image analysis algorithm based on a Circular-Hough-Transformation, as described in detail in [46,47]. Log-normal size distributions with geometric standard deviations of about 1.34 and 1.47, depending on the soot system, were fitted to the data to derive the count median diameter (CMD). Nanostructure analysis was performed by fringe evaluation using an image pattern algorithm [46,47], from which the distribution of the fringe lengths was obtained, and the mean of this distribution (Λ_{mean}) as well as the ninth decile (Λ_{90}) were calculated. Further details on the fringe analysis workflow are reported in the Supplementary Material (Fig. S1).

A PHI 5000 Versa Probe equipment with a monochromatic Al k-alpha X-ray source (1486.6 eV) was employed to carry out X-ray photoelectron spectroscopy (XPS) measurements. The high-resolution spectra were charge-corrected with respect to the C 1 s peak at 284.8 eV.

Temperature programmed desorption (TPD) analyses were carried out in an Altamira Ami-300Lite equipped with a thermal conductivity detector (TCD). NH_3 and CO_2 were used to study the surface acidity and basicity, while the oxygen storage capacity was compared by performing O_2-TPD. The catalyst powder (100 mg) was pretreated in He at 550 °C for 30 min, then saturated with pure O_2 at this temperature for 30 min (O_2-TPD), or cooled and saturated for 60 min under a flow of 10 vol% NH_3 in He at 100 °C (NH_3-TPD), or under a flow of pure CO_2 at 50 °C (CO_2-TPD). After a 30 min He flush, the TPD analysis was performed under a 25 mL min^{-1} He flow, by heating the sample from 100 to 600 °C with a 10 °C min^{-1} ramp.

2.3. Activity tests

Two approaches were employed to quantify activity: temperature-programmed oxidation (TPO) was performed for both catalytic and non-catalytic soot oxidation, while thermogravimetric analysis (TGA) was used to determine kinetic parameter sets of the initial soot types and to assess catalyst stability.

The activity of the catalysts towards the oxidation of the various soot samples was assessed through TPO tests. A catalytic bed containing 45 mg of catalyst, 5 mg of soot, and 150 mg of SiO_2 (Sigma-Aldrich) was placed in a quartz U-tube reactor, close to a K-type thermocouple, and then inserted in a PID-controlled furnace. Two different degrees of contact were considered: tight contact (TC) conditions were achieved by mixing the solid powders in a ball mill (15 min at 290 rpm), while loose contact (LC) conditions were reached by gently mixing the powders for few minutes using a spatula. During the test, a mixture with 10 vol% of O_2 in N_2 (100 mL min^{-1}) was sent to the reactor. After a pre-treatment at 100 °C for 30 min, the temperature was raised from 100 up to 700 °C with a 5 °C min^{-1} ramp, while continuously monitoring the CO and CO_2 concentrations in the reactor outlet using an ABB AO2020 infrared gas analyzer. CO selectivity was calculated as the ratio between the total amount of CO produced during the test and the total amount of $CO+CO_2$ formed. Blank tests of soot oxidation were carried out by inserting only silica and soot in the reactor, after gently mixing them with a spatula.

TGA was employed for the initial soot samples to determine kinetic parameter sets. Measurements were conducted with a TG 209 F1 Libra (Netzsch Gerätebau GmbH) under non-isothermal conditions. About 2.0 ± 0.2 mg of soot were heated from ambient temperature to 1000 °C at a rate of 5 °C min^{-1} in 10 vol% O_2 in N_2 at ambient pressure and a total flow rate of 0.1 L min^{-1}. The resulting profiles were analyzed by non-linear regression using a single-step kinetic model with Arrhenius-type temperature dependence, as described in [47] and in SI.

Catalyst degradation was investigated in the same way. Catalyst-soot mixtures with a 1:1 mass ratio were subjected to ten consecutive non-isothermal TGA runs up to 700 °C, each time with fresh soot added to the recovered catalyst. After every run, the apparent activation energy was determined to quantify the progressive loss of catalytic activity.

2.4. Tracking catalyst-soot interfaces by stepwise oxidation

Stepwise oxidation experiments were performed to investigate the structural evolution at catalyst-soot interfaces. The methodology, reported in [59], involves preparing soot-catalyst suspensions in water, followed by drop-casting on high-temperature SiO_2 TEM grids and subsequent drying prior to oxidation experiments. Selected catalyst-soot interfaces were first analyzed by HRTEM (see Section 2.2) and their exact positions on the grid were recorded for re-identification. The grids were then subjected to consecutive ex-situ oxidation steps of 200 s in the TGA (see Section 2.3), at 575 °C in 10 vol% O_2 in N_2. This temperature was chosen as a compromise between grid stability and sufficiently resolvable oxidation kinetics. After each oxidation step, the same catalyst-soot interfaces were re-identified and reanalyzed by HRTEM. This approach allowed direct tracking of the evolution of catalyst-soot interfaces and provided insights into restructuring processes during oxidation.

3. Results and discussion

3.1. Structural and textural properties of the catalysts

All the catalysts were obtained using the same hydrothermal synthesis procedure. However, as shown by the FESEM micrographs in Fig. 1, the addition of Pr and La significantly affected the ripening process of the crystals and the final morphology of the powder. While pure ceria consists of cubic nanoparticles, the incorporation of Pr and La ions modifies the relative growth rates of specific crystallographic planes, promoting anisotropic growth and leading to the formation of rod-like structures in addition to nanocubes in the doped catalysts. Energy dispersive X-ray spectroscopy confirmed that the actual composition of the mixed oxides matches the nominal composition. However, previous investigations on the Ce50La50 sample revealed that nanocubes are richer in Ce while rod-like particles contain a relatively higher amount of lanthanum [38].

The X-ray diffractograms of the synthesized catalysts are displayed in

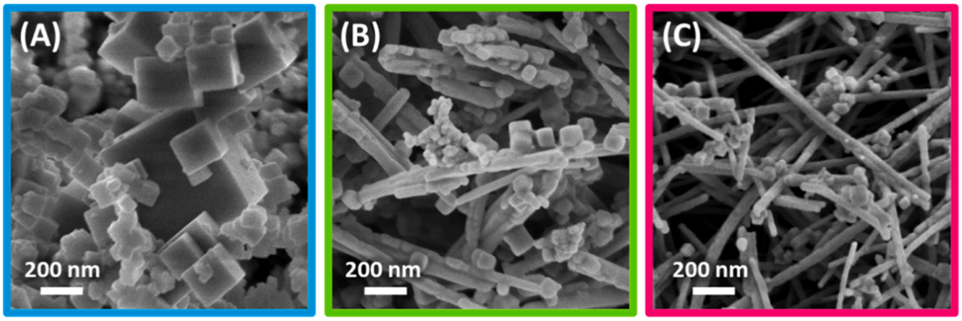

Fig. 1. FESEM images of the synthesized catalysts: CeO_2 (A), Ce50Pr50 (B), and Ce50La50 (C).

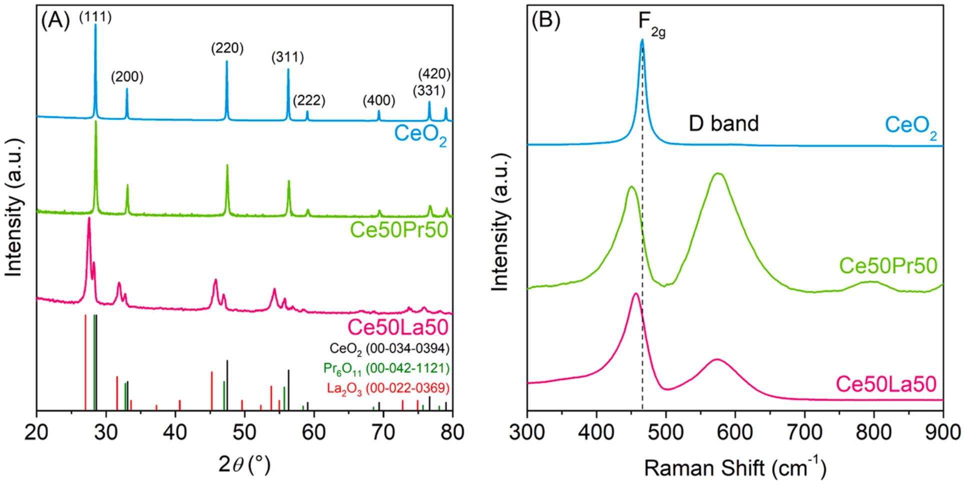

Fig. 2. X-ray diffractograms (A) and Raman spectra (B) of the synthesized catalysts. Reference diffraction patterns of pure oxides obtained from the ICDD database are included for comparison. Raman spectra were normalized with respect to the intensity of ceria F_{2g} peak.

Fig. 2A. The eight sharp peaks in the CeO_2 profile correspond to the fluorite crystal structure typical of ceria [60,61]. The Ce50Pr50 pattern features the same reflections, indicating that Pr ions are well incorporated in ceria lattice [62,63]. However, the latter sample shows slightly broader peaks, associated with a smaller average size of the crystallites (see Table 1). This effect is even more visible for Ce50La50, and it is accompanied by splitting of the fluorite peaks. As shown in Fig. 2A, each pair of peaks is located between the characteristic features of pure CeO_2 and La_2O_3 patterns, suggesting the formation of two Ce-La solid solutions. A similar splitting behavior has been previously ascribed to a bimodal distribution of the fluorite unit cell size, i.e. to the presence of two main mixed phases showing the same type of cubic fluorite structure but with different lattice parameters [38]. In particular, Ce-rich nanocubes (NC) contain smaller cations (mainly Ce^{4+}) and are hence characterized by a smaller unit cell size, corresponding to the right-hand series of peaks in the XRD pattern. Instead, La-rich nanorods (NR), containing larger La^{3+} cations, show an expanded unit cell size and give rise to a second series of peaks shifted towards lower diffraction angles. The smaller crystallite size in the doped materials is likely due to crystal growth inhibition in the presence of Pr or La ions. This results in a higher specific surface area for the mixed catalysts, as reported in Table 1, and in a lower average pore diameters, as the pores in these materials arise primarily from interparticle voids (N_2 physisorption isotherms are reported in Fig. S2).

Fig. 2B reports the Raman spectra of the synthesized catalysts. All the samples exhibit the typical F_{2g} peak arising from the symmetric stretching mode of the cerium-oxygen bonds in the fluorite structure of ceria [64,65]. This component, however, presents a significant shift, from 465 cm^{-1} for CeO_2 to 457 cm^{-1} for Ce50La50 and 451 cm^{-1} for Ce50Pr50. It also becomes broader and asymmetric in the mixed oxides, with a low frequency tail. These changes are related to the incorporation of Pr and La ions, which causes distortion in the anion framework

Table 1
Structural and textural properties of the synthesized catalysts.

Catalyst	**Crystallite size**[a] (nm)	**Unit cell size**[a] (nm)	**SSA**[b]($m^2\ g^{-1}$)	$\mathbf{V_p}$[b]($cm^3\ g^{-1}$)	$\mathbf{D_p}$[b](nm)	**Raman D/F_{2g} ratio**(-)
CeO_2	169	0.5412	6.3	0.029	24	0.03
Ce50Pr50	50	0.5406	7.9	0.026	18	2.15
Ce50La50 – NC[c]	32	0.5462	10.8	0.034	16	0.87
Ce50La50 – NR[c]	15	0.5593				

[a] The average crystallite size and the unit cell size were estimated using XRD data.

[b] The specific surface area (SSA), the total pore volume (V_p) and the average pore diameter (D_p) were measured through N_2-physisorption (isotherms reported in Fig. S2).

[c] For Ce50La50 the crystal properties were determined separately for the nanocube (NC) and nanorod (NR) phases, using the right and left series of diffraction peaks, respectively.

symmetry of ceria [37]. Structural alteration is also evidenced by the increased intensity of the D band in the 550 – 600 cm^{-1} range, which is related to the presence of different types of lattice defects, such as Frenkel sites and oxygen vacancies [58,66]. Vacancies can indeed form upon substitution of Ce^{4+} by Pr^{3+} or La^{3+} ions [37]. The D/F_{2g} ratio between the areas of the D band and the F_{2g} peak is particularly high for Ce50Pr50 (Table 1); nevertheless, in addition to defect formation, other phenomena are likely to contribute to this result, albeit to a lesser extent [67]. Firstly, some Pr^{4+}-containing sites have been claimed to give rise to a resonance Raman effect, which would strongly increase the signal at 570 cm^{-1} [68]. Secondly, the dark color of Pr-doped ceria entails a reduction of the light penetration depth, limiting Raman measurements to more superficial regions, which are naturally more defective than the bulk [69].

3.2. Chemical properties of the catalyst surface

The acidity and basicity of the catalyst surface were investigated via NH_3-TPD and CO_2-TPD, respectively. The thus-obtained desorption profiles, displayed in Fig. 3, provide information about the quantity and strength of the acidic/basic sites (see Table 2). The NH_3-TPD profile of pure CeO_2 is almost flat (Fig. 3A), indicating a lack of acid sites on this oxide, which is indeed generally considered to be predominantly basic [70]. Instead, intense ammonia desorption bands between 150 and 500 °C were clearly detected for Ce50Pr50 and Ce50La50, revealing the presence of medium-strong acid sites at the catalyst surface [71,72]. These sites are slightly stronger and significantly more abundant for Ce50La50 (Table 2), and according to previous literature can be mainly assigned to Lewis acid sites [70,73–75]. Consistently, FTIR analysis of pyridine adsorption on the catalysts confirmed the prevalence of Lewis sites on Brønsted sites [76] (see Fig. S3). For reference, La-doped ceria exhibits an acid site density (107 $\mu mol_{NH3}\ g_{cat}^{-1}$) comparable to that measured for alumina-based materials and Ce-modified alumina (20 – 200 $\mu mol_{NH3}\ g_{cat}^{-1}$) [77,78], but significantly lower than that typically reported for strongly acidic supports such as zeolites (300 – 1000 $\mu mol_{NH3}\ g_{cat}^{-1}$) [79–81].

All the CO_2-TPD profiles in Fig. 3B feature a first desorption peak centered at 100 °C, which signals the presence of weak basic sites in all the catalysts. Furthermore, Ce50Pr50 profile also shows an additional band in the 200 – 350 °C range, resulting from basic sites with intermediate strength, such as O^{2-} sites that can form monodentate carbonates upon interaction with CO_2 [82]. The remarkable desorption peak above 250 °C reveals instead that Ce50La50 is rich in medium-strong basic sites (Table 2), which can form rather stable bidentate and polydentate-like carbonates [82].

Table 2
Density of acid and basic sites (expressed as probe molecule adsorption capacity per unit of catalyst mass) estimated from NH_3-TPD and CO_2-TPD, and quantity of oxygen released during O_2-TPD.

Catalyst	Density of acid sites ($\mu mol_{NH3}\ g_{cat}^{-1}$)	Density of basic sites ($\mu mol_{CO2}\ g_{cat}^{-1}$)	Oxygen released ($\mu mol_{O2}\ g_{cat}^{-1}$)
CeO_2	11	7	9
Ce50Pr50	49	16	227
Ce50La50	107	63	28

The oxygen storage capacity of the three ceria-based catalysts was evaluated through O_2-TPD, whose results are visible in Fig. 3 C. Doping significantly increases the quantity of oxygen that ceria can release up to 550 °C (see Table 2). The incorporation of La^{3+} ions in ceria structure can be expected to create oxygen vacancies (as confirmed by Raman spectroscopy), which can weaken the Ce – O bonds and facilitate oxygen mobility from the bulk to the surface [83]. However, a much more intense increase of oxygen storage capacity (ca. 25 times) was detected in the case of Ce50Pr50, likely due to the coupling of Ce^{3+}/Ce^{4+} and Pr^{3+}/Pr^{4+} redox cycles, with praseodymium being more reducible than cerium [39,67,84]. Interestingly, distinct O_2 desorption features were observed for the two mixed oxides. The main oxygen release peak around 300 °C for Ce50La50 can be attributed to surface active oxygen species, as also supported by XPS results (see below). In contrast, the higher temperature of the main peak observed for Ce50Pr50 suggests that this is also associated with the release of sub-surface lattice oxygen, which is less directly involved in surface reactions [85,86].

The synthesized catalysts were further investigated through XPS, to gain insights into the chemical states of the elements in the surface. The XPS spectra are reported in Fig. S4, while the results from deconvolution are summarized in Table 3. Concerning the O 1 s core level (Fig. S4 A-C), two main peaks were detected for all the catalysts: a first component at 529.0 eV (slightly shifted at 528.3–528.4 eV in the doped samples [87, 88]) is related to lattice oxygen (O_β), while a second peak at 531.1–531.3 eV corresponds instead to surface capping oxygen species (O_α), which can include hydroxyls (OH^-) and highly reactive superoxide

Table 3
Relative abundance of the different surface chemical species as detected by XPS.

Catalyst	Oxygen species (%)			Cerium species (%)		Praseodymium species (%)	
	O_α	O_β	O_γ	Ce^{3+}	Ce^{4+}	Pr^{3+}	Pr^{4+}
CeO_2	28.1	67.7	4.2	22.1	77.9	-	-
Ce50Pr50	37.8	58.0	4.2	23.0	76.0	71.8	28.2
Ce50La50	58.8	32.7	8.5	25.7	74.3	-	-

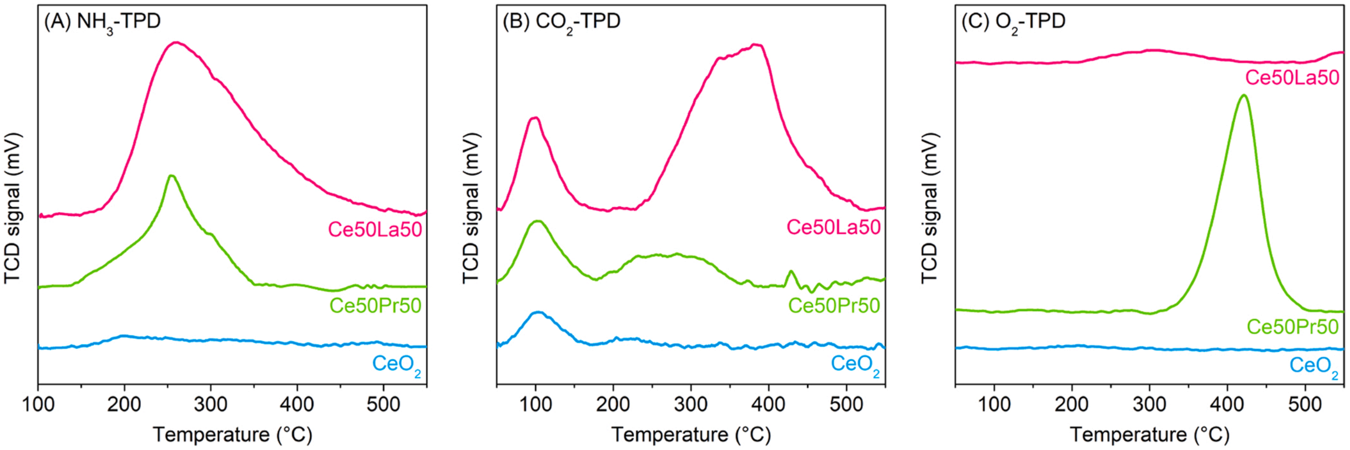

Fig. 3. NH_3-TPD (A), CO_2-TPD (B), and O_2-TPD (C) profiles of the synthesized catalysts. All the curves started from 0 mV but were vertically shifted for the sake of clarity.

(O_2^-) or peroxide (O_2^{2-}) ions [89–91]. A third less intense shoulder at 533.4–534.8 eV was also detected (O_γ), likely due to traces of adventitious species such as adsorbed water, carbonates or formates [85,92,93]. As visible in Table 3, the two doped catalysts feature a significantly higher quantity of O_α and O_γ species at their surface with respect to pristine ceria, especially in the case of La doping. This is consistent with the O_2-TPD results, showing a significant release of labile oxygen species at medium-low temperature for Ce50La50. Since these O_α and O_γ species can promote oxygen spillover and play a role during catalytic oxidation, their increased presence might be associated with enhanced soot oxidation activity [22,88,94].

From the deconvolution of the Ce 3d XPS spectra, ten peaks can be identified: six of these can be ascribed to Ce^{4+} ions, while the remaining four are related to the Ce^{3+} oxidation state (Fig. S4 D-F) [22,93,95]. A similar 10-peaks approach can be used for the deconvolution of Pr 3d core level too (Fig. S4 G) [67,96]. A slight increase in the quantity of reduced cerium was observed upon doping (from 22% to ca. 23–26%, Table 3), likely due to better compatibility of this state with the trivalent ions of La and Pr. Accordingly, Pr^{3+} is the main praseodymium species in the Ce50Pr50 sample (71.8%), in line with the higher reducibility of this element with respect to cerium [67]. The abundance of reduced cations and oxygen vacancies at the surface can be associated with promoted O_2 activation and Mars-van Krevelen mechanism [26,27].

Finally, the La 3d XPS spectrum of Ce50La50 is characterized by two separate groups of peaks related to the La $3d_{5/2}$ and La $3d_{3/2}$ levels (Fig. S4 H). The central peak in the La $3d_{5/2}$ region falls at 834.3 eV and is characterized by a spin-orbit splitting of 16.8 eV with the corresponding La $3d_{3/2}$ component, which is typical of the La_2O_3 phase [97]. However, while pure La_2O_3 only exhibits two couples of peaks, deriving from multiplet splitting, an additional couple of peaks at lower binding energies was detected in Ce50La50, likely arising from La in strong interaction with ceria within the mixed oxide (La–O–Ce) or bonded to OH and other O_α species [38,98]. Finally, two La LMM Auger peaks are also visible in the spectrum.

3.3. *Structural and textural properties of soot*

The structural and textural properties of the different soot types are summarized in Table 4, while representative HRTEM images are reported in Fig. S5. Nanostructure analysis, performed according to the workflow reported in the Supplementary Material (Fig. S1), shows that the mean and the ninth decile of the fringe length distribution scale closely, indicating that both parameters reflect the same structural trend. The fringes represent polyaromatic clusters that constitute the basic building blocks of the primary soot particles, and their length is strongly linked to the C/H ratio: longer fringes reflect more condensed aromatic structures with fewer hydrogen-terminated edge sites [99]. On the particle level, a clear relation emerges between size and nanostructure, as soot with a larger count median diameter (CMD) tends to exhibit longer graphene-like fringes, consistent with previous observations [47]. In contrast, the specific surface area does not scale with CMD or other particle-level metrics, since SSA is governed by the fractal aggregate morphology rather than by primary particle size alone. Together, the results reveal a diverse set of structural and textural characteristics, suggesting that the reactivity of the different soot types toward oxidation can be expected to vary accordingly [46].

3.4. *Reactivity of the initial soot samples*

The reactivity of the initial soot samples was studied with a double approach, including TGA and TPO tests. TGA profiles were employed to determine the apparent activation energy of soot oxidation (see Table 4), following the method described in [47] and in SI. At the same time, TPO tests were carried out without catalyst addition, monitoring CO and CO_2 evolution during non-catalytic oxidation. As shown in Fig. 4 and S6, the CO and CO_2 profiles follow the expected trends, in line with earlier demonstrations that TPO reflects TGA results [45]. For all soot types, the selectivity toward CO_2 is limited, with nearly half of the carbon oxidized to CO. The position of the CO and CO_2 emission maxima as a function of temperature reflects the intrinsic reactivity of the soot types: peaks at lower temperatures indicate higher reactivity, whereas peaks shifted to higher temperatures correspond to lower reactivity. MFS-C_2H_2 showed CO and CO_2 emission peaks at the lowest temperatures, consistent with its lowest activation energy of 143 kJ mol^{-1} whereas CB-SB250 peaked at the highest temperatures above 650 °C, in line with its highest activation energy of 162 kJ mol^{-1}. The other samples fell in between, with activation energies of 146 kJ mol^{-1} for MFS-$T10_{3bar}$ and CB-S170, and 154 kJ mol^{-1} for CB-P90. Removing surface polycyclic aromatic hydrocarbons (PAHs) from MFS-C_2H_2 by DCM extraction shifted the CO_X emission peak maximum by about 50 °C toward higher temperatures (see Fig. S6), while the overall profile shape remained unchanged. This indicates that extractable surface species, most likely adsorbed PAHs, contribute to the onset and moderate temperature shift of oxidation, while the nearly unchanged profile shape suggests that the oxidation pathway of the underlying soot nanostructure remains unaffected.

When comparing these results with the structural parameters summarized in Table 4, a clear pattern emerges. Soot particles with extended fringes exhibit higher apparent activation energies and thus lower reactivity, in line with earlier findings that nanostructural order determines the soot oxidation process [46,47,59]. The same trend is reflected in the C/H ratio, as structures with longer graphene-like fringes and fewer hydrogen-terminated edge sites require higher temperatures for oxidation. The primary particle size distribution reflected in the CMD also follows this behavior, as smaller particles tend to show shorter fringes and lower apparent activation energies [47], i.e., they are more reactive. In contrast, the BET SSA does not show a systematic trend with reactivity in the present dataset. This suggests that the measured total SSA, largely governed by aggregate morphology and pore accessibility, is not by itself a sufficient descriptor for the intrinsic oxidation rate. Instead, nanostructural metrics such as fringe length distributions and the atomic C/H ratio appear to be more decisive.

3.5. *Catalytic oxidation of soot samples*

To cover a wide range of particle properties and reactivity, catalytic oxidation experiments with the three catalysts were performed with one MFS sample, i.e., MFS-C_2H_2, together with the three CB samples. Two

Table 4
Properties of different soot types, including count median diameter (CMD), specific surface area (SSA), mean fringe length (Λ_{mean}), 90th percentile fringe length (Λ_{90}), atomic C/H ratio, and apparent activation energy.

Soot type	**CMD**(nm)	**SSA**(m^2 g^{-1})	$\mathbf{\Lambda_{mean}}$(Å)	$\mathbf{\Lambda_{90}}$(Å)	**C/H ratio**(-)	**Activation Energy**(kJ mol^{-1})
MFS-C_2H_2[a]	16	96	5.2	7.1	8.0	143
MFS-$T10_{3bar}$	25	68	5.1	7.4	6.0	146
CB-SB250	42	48	6.6	9.9	20.0	162
CB-P90	23	293	5.5	8.1	17.0	154
CB-S170	18	263	5.2	7.1	8.7	146

[a] Soot particle properties of Soxhlet-extracted via DCM soot particles, referred to as MFS-C_2H_2 (DCM extracted), are identical.

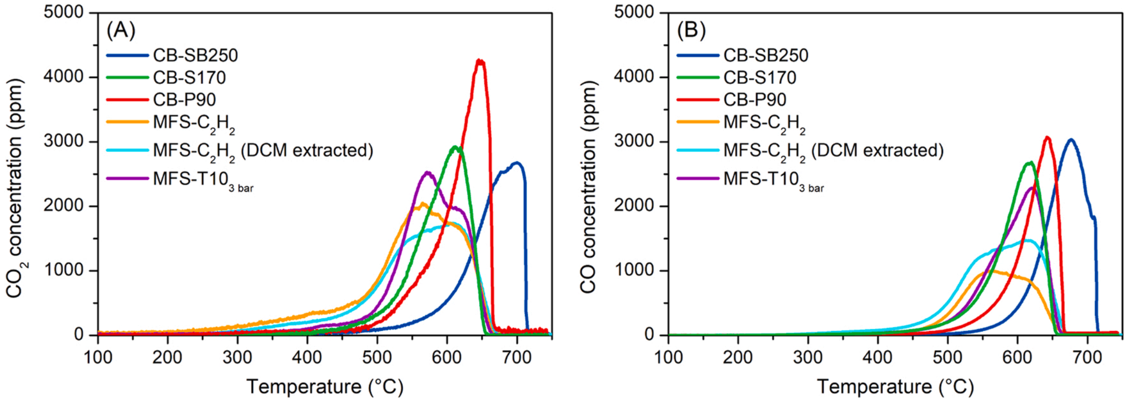

Fig. 4. Evolution of the concentration of CO_2 (A) and CO (B) at the outlet of the reactor during non-catalytic oxidation of the soot samples.

degrees of contact between catalyst and soot were probed: loose contact (LC) was obtained through gently mixing the two powders, while tight contact (TC) was achieved in a ball mill. LC is considered more representative of actual operating conditions in catalytic particulate filters, where soot is deposited along the filter channels with limited physical contact; in this case, the number of contact points mainly depends on the catalyst morphology and specific surface area [39]. Conversely, TC aims to create numerous and intimate contact points between the solid particles, so to assess the intrinsic activity of the catalyst, avoiding mass transfer limitations [36].

The soot conversion curves obtained during the catalytic tests are displayed in Fig. 5, while the profiles of CO and CO_2 concentration in the outlet are reported in Fig. S7-S10. As shown by the comparison with uncatalyzed tests in LC, the presence of a catalyst always allowed to reduce the temperature required for soot oxidation, confirming the suitability of ceria-based materials for this application. However, the catalyst efficiency is highly dependent on the degree of contact between catalyst and soot. In LC, the transfer of reactive oxygen from the catalyst to the soot particles is hindered due to the lower number of contact points, leading to a wider temperature range for complete oxidation. Conversely, in TC active oxygen species can efficiently migrate to the soot surface, and soot itself can act as a driving force for extracting lattice oxygen, promoting the MvK-like mechanism [39]. As a result, intimate contact leads to significantly lower soot oxidation temperatures, as clearly shown in Fig. 6 reporting the T50% obtained in the different tests, i.e., the temperatures required for reaching 50% of soot conversion by mass.

Interestingly, the catalytic activity trend observed for the three catalysts, i.e., CeO_2 < Ce50Pr50 < Ce50La50, remained consistent regardless of the soot type or contact mode. The systematic enhancement in catalytic performance upon Pr and La addition arises from the combination of various factors. First, the different morphology can contribute to the superior activity of Ce50Pr50 and Ce50La50 in LC, as their rod-like structures can better host soot particles with respect to ceria nanocubes. This results in an increased quantity of effective solid-solid contact points, thanks to enhanced physical contact efficiency and improved accessibility of the catalyst active sites to soot particles [100]. Moreover, as evidenced by O_2-TPD, rare earth elements like Pr and La

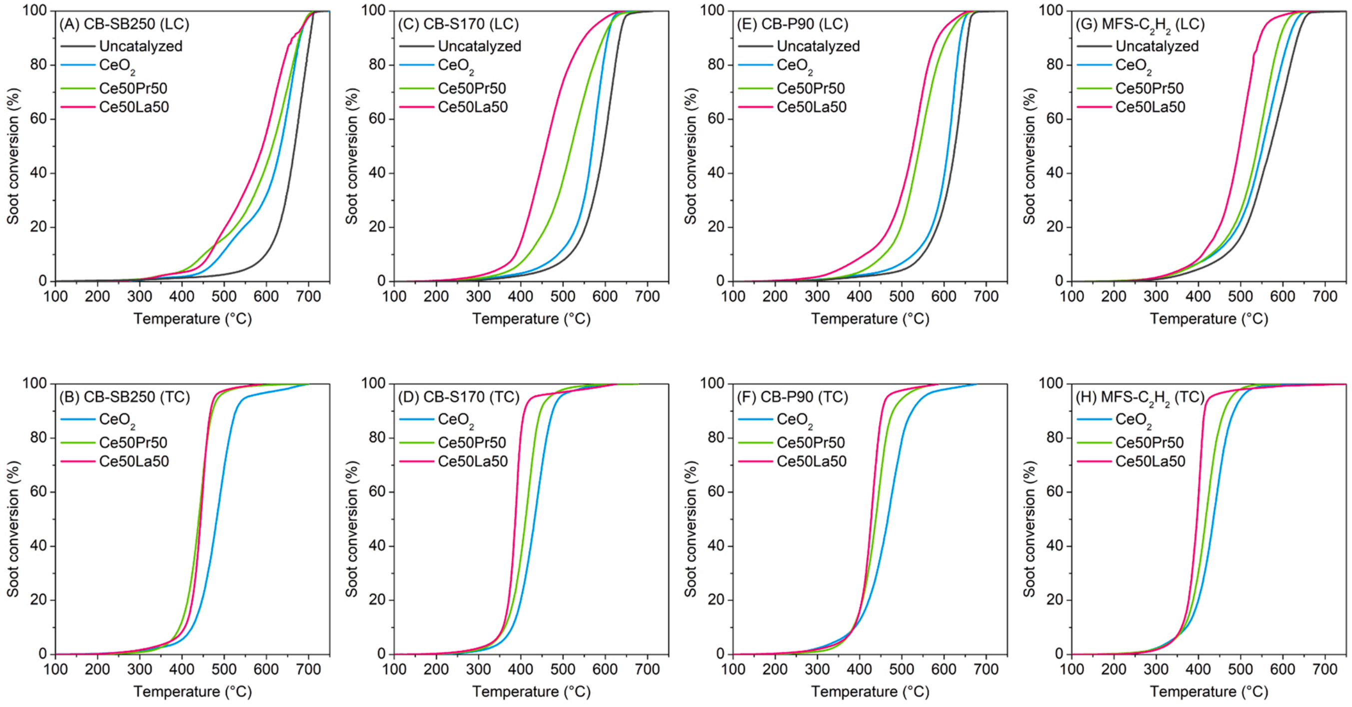

Fig. 5. Conversion curves as a function of the temperature resulting from the catalytic oxidation of the different soot samples: CB-SB250 in LC (A) and TC (B), CB-S170 in LC (C) and TC (D), CB-P90 in LC (E) and TC (F), MFS-C_2H_2 in LC (G) and TC (H).

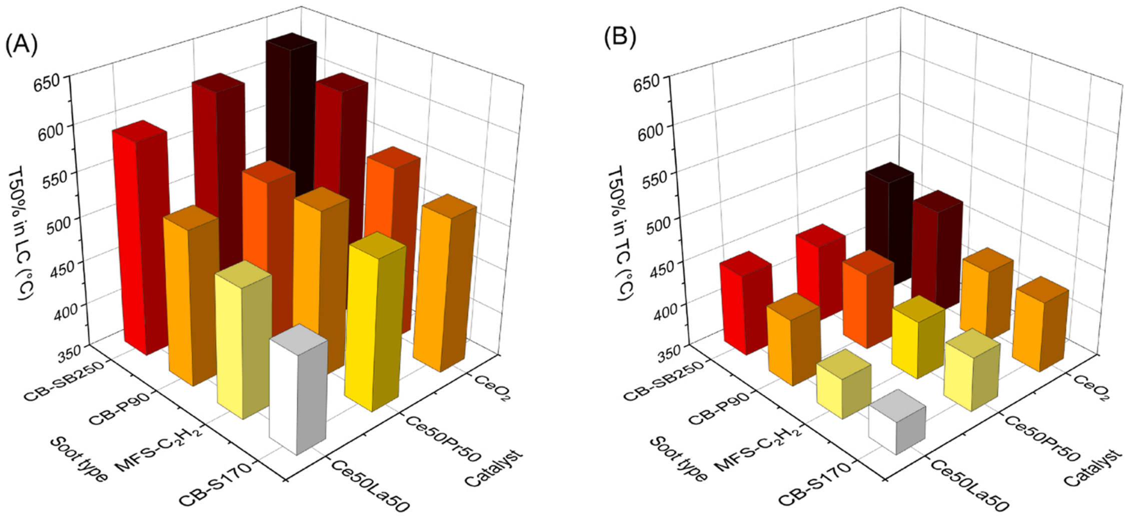

Fig. 6. Evolution of the T50% temperature as a function of the type of soot and catalyst in LC (A) and TC (B).

can significantly improve the oxygen storage and release capacity of ceria, as well as the redox properties of the oxide. This could also account for the higher abundance of capping oxygen species revealed by XPS (Table 3), which have a primary role in soot oxidation. At the same time, the increased surface acidity of the two mixed samples is also a relevant factor (see Table 2). The presence of medium-strong Lewis acid sites can indeed promote the formation of highly reactive carbocation intermediates through electronic interactions at the soot-catalyst interface [81,101]. These unstable species can then easily react with oxygen from either the gas phase or the catalyst lattice, contributing to effective soot conversion at lower temperatures. Consistently, an inverse correlation could be found between the concentration of acid sites and the T50%, as depicted in Fig. 7A, proving that surface acidity has a positive and tangible impact on soot oxidation. A similar trend was observed when comparing T50% with the density of basic sites (Fig. 7B), suggesting that these centers may also play a role in promoting catalytic activity [17].

While exhibiting the best soot oxidation activity, the Ce50La50 sample also showed the highest CO selectivity (ranging from 3% to 13%, as visible in Fig. S11) compared to the other catalysts. This behavior can be attributed to the increased basicity of the Ce50La50 sample, as revealed by CO_2-TPD (Table 2). The presence of strong basic sites is associated with the formation of rather stable carbonate-like species, and this hinders the desorption of CO_2 from the catalyst surface, slowing down the reaction rate of CO to CO_2 oxidation [88]. In fact, the conversion of carbonates into physisorbed CO_2 has been identified as the rate-determining step of the carbonate-mediated Mars-van Krevelen mechanism for CO oxidation over rare earth-doped ceria [102]. Consequently, the presence of stronger basic sites is expected to raise the energy barrier of this step, thereby hindering the overall CO oxidation rate. Instead, the Ce50Pr50 sample generally exhibits the lowest CO selectivity (0.5% – 5%). While the intermediate basicity of this catalyst may hinder CO_2 desorption, the high oxygen storage capacity and reducibility of Ce50Pr50 promote CO oxidation [56]. As a result, for Ce50Pr50 the positive effect of oxygen availability exceeds the influence of basicity, leading to lower CO selectivity.

When comparing the reactivity of the different soot samples, a consistent trend was observed, irrespective of the catalyst: CB-SB250 <CB-P90 < MFS-C_2H_2 < CB-S170 (Figs. 5 and 6). This order agrees with the intrinsic reactivity derived from non-catalytic TPO (see Section 3.3), confirming that the physicochemical properties of soot dominate the oxidation process. Soot reactivity is mainly governed by nanostructural order, and thus the C/H ratio, with shorter fringes embedded within primary particles being more reactive, i.e., less

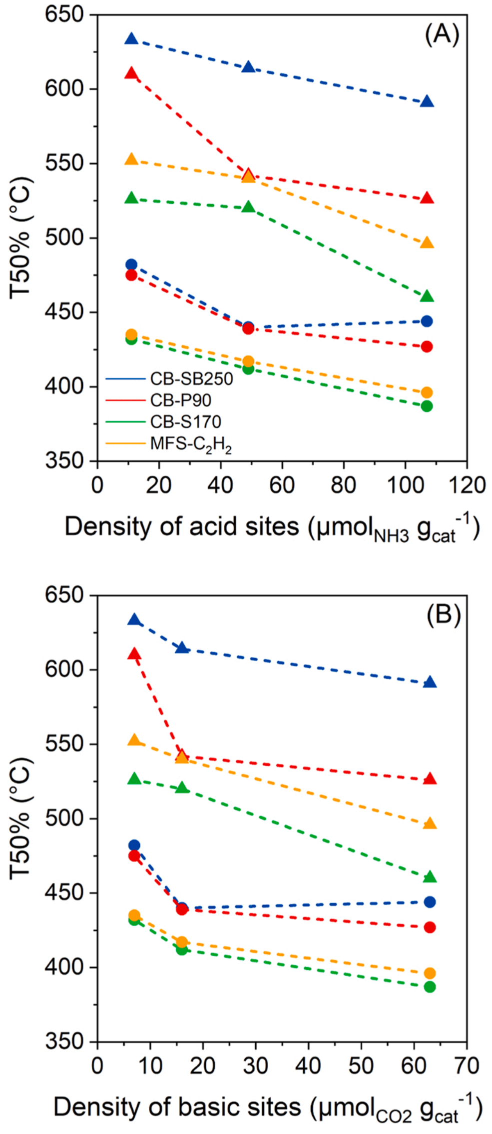

Fig. 7. Evolution of the T50% measured during catalytic oxidation of the different soot samples in loose contact (triangles) and tight contact (circles) as a function of the density of acid sites (A) and basic sites (B) at the catalyst surface.

graphitic structures showing higher reactivity.

Between MFS-C_2H_2 and CB-S170, the structural parameters are strikingly similar: CMD of the primary particle size distribution of 16 nm versus 18 nm, mean fringe length of 5.2 Å for both, and C/H ratios of 8.0 versus 8.7 (see Table 4). The only pronounced difference is the specific surface area, amounting to 96 $m^2\,g^{-1}$ and 263 $m^2\,g^{-1}$, respectively. This difference may explain why CB-S170 exhibits higher reactivity than MFS-C_2H_2 in the presence of catalysts, in contrast to the uncatalyzed conditions. The larger specific surface area of CB-S170 likely facilitates more effective soot-catalyst-contact, which could account for its higher reactivity under catalytic conditions despite otherwise comparable intrinsic properties.

The impact of contact mode was also modulated by the catalyst composition. Notably, Ce50La50 was most effective at minimizing the performance gap between LC and TC, as shown by the reduced difference in T10% and T50% between the two contact modes (illustrated in Fig. 8). This behavior suggests that this catalyst is particularly effective at interacting with soot and promoting its oxidation even when physical contact between the catalyst and soot is limited. As will be shown in the next section, stepwise oxidation experiments with HRTEM tracking of catalyst-soot interfaces demonstrate that this catalyst can restructure during oxidation, forming new contact points that are particularly beneficial under LC conditions where contact is limited.

3.6. *Tracking catalyst-soot interface evolution by stepwise oxidation and HRTEM and its implications for stability*

The structural evolution of soot-catalyst interfaces during oxidation was investigated by stepwise oxidation experiments combined with repeated HRTEM analysis. After each oxidation step, the same catalyst-soot regions were re-imaged by HRTEM, allowing direct visualization of the progressive oxidation of soot and possible restructuring of the catalyst. CeO_2 and Ce50La50 were selected as representative catalysts: CeO_2 as a reference with stable cubic morphology and lower activity, and Ce50La50 as the most active catalyst. Among the soot samples, MFS-C_2H_2 was chosen because it most closely resembles engine soot and contains PAHs adsorbed on its surface [46,47].

Fig. 9 shows the CeO_2/MFS-C_2H_2 system during stepwise oxidation. The high-contrast regions in HRTEM images correspond to CeO_2 nanoparticles, while the surrounding areas of lower contrast represent soot aggregates. Colored arrows were added to facilitate the identification of the same catalyst-soot contact regions across the image sequence. The catalyst particles preserve their cubic morphology and remain at their initial positions throughout the oxidation sequence. A progressive thinning of the soot around the CeO_2 particle surface was observed, demonstrating how oxidation proceeds directly at the catalyst-soot interface. As the reaction progresses, small soot bridges, marked by the red dotted arrows, remain temporarily attached to the catalyst before being consumed, while the yellow dotted arrows indicate the gradual emergence of fully exposed catalyst surfaces. In contrast, adjacent soot regions, highlighted by the white dashed contours, persist and undergo slower non-catalytic oxidation. These observations confirm that soot is preferentially oxidized at catalyst-soot interfaces, but that CeO_2 particles do not restructure to generate new contact points. This limited ability to renew interfaces contributes to the comparatively lower catalytic activity of CeO_2. However, it is not the only reason: the weaker acid-base properties and lower oxygen storage and release capacity of pure ceria also limit its reactivity compared to the mixed oxides.

Fig. 10 shows the Ce50La50/MFS-C_2H_2 system during stepwise oxidation. Nanocubes amidst rod-like structures, initially embedded within soot aggregates, reorganize into clusters as oxidation progresses (see image series in the middle). In this oxidation sequence, soot aggregates and catalyst particles can only be tracked to a limited extent, as the restructuring continuously transports new catalyst particles into the field of view, as exemplified by the catalyst particle marked by the yellow arrow in the right image of the middle series. This particle newly enters the field of view next to other catalyst particles, such as the one highlighted by the red contour, that remained within the field of view throughout the sequence. This restructuring creates new contact sites with the surrounding soot, allowing oxidation to proceed beyond the initially accessible interfaces. As soot adjacent to the catalyst is consumed and clean surfaces appear, new regions of the deposited soot layer come into contact and are subsequently oxidized. Indeed, as shown in the lower right image in Fig. 10, the little soot remaining after multiple oxidation cycles is still in contact with the catalyst surface, as indicated by the dotted blue arrow. These observations demonstrate that Ce50La50 can dynamically adapt its contact with soot, which is particularly advantageous under LC conditions where interactions are otherwise limited.

The restructuring processes observed by HRTEM are consistent with the degradation behavior measured in repeated TGA experiments. In TC with CB-S170, CeO_2 quickly reached stable apparent activation energies after approximately five oxidation cycles, reflecting a relatively fast loss of activity, as shown in Table S1. Ce50Pr50 shows the same behavior. Ce50La50, in contrast, retains higher activity over a longer period, requiring around ten cycles before stabilization. However, it also shows the largest relative increase in apparent activation energy of about 13%, approximately twice the increase observed for CeO_2 and Ce50Pr50 (see Table S1). This trend is consistent with the surface area loss caused by clustering. Together, these results highlight the dual role of Ce50La50 restructuring: it enables high activity by creating new soot-catalyst interfaces, but at the expense of long-term stability.

Restructuring, however, is only one element contributing to the superior performance of Ce50La50: the high density of acid sites, enhanced oxygen storage and release capacity, and the mixed morphology of nanocubes and rods are equally decisive. In particular, the continuous regeneration of soot-catalyst contact points can be

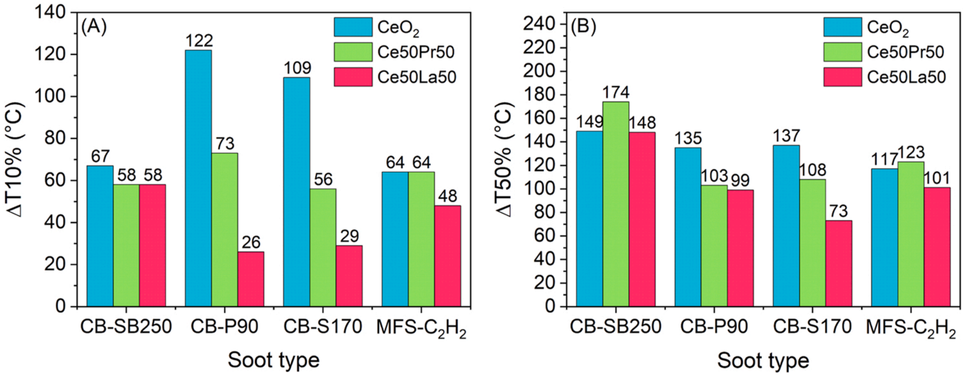

Fig. 8. Difference between the soot oxidation temperatures measured during catalytic tests in loose and tight contact, considering T10% (A) and T50% (B).

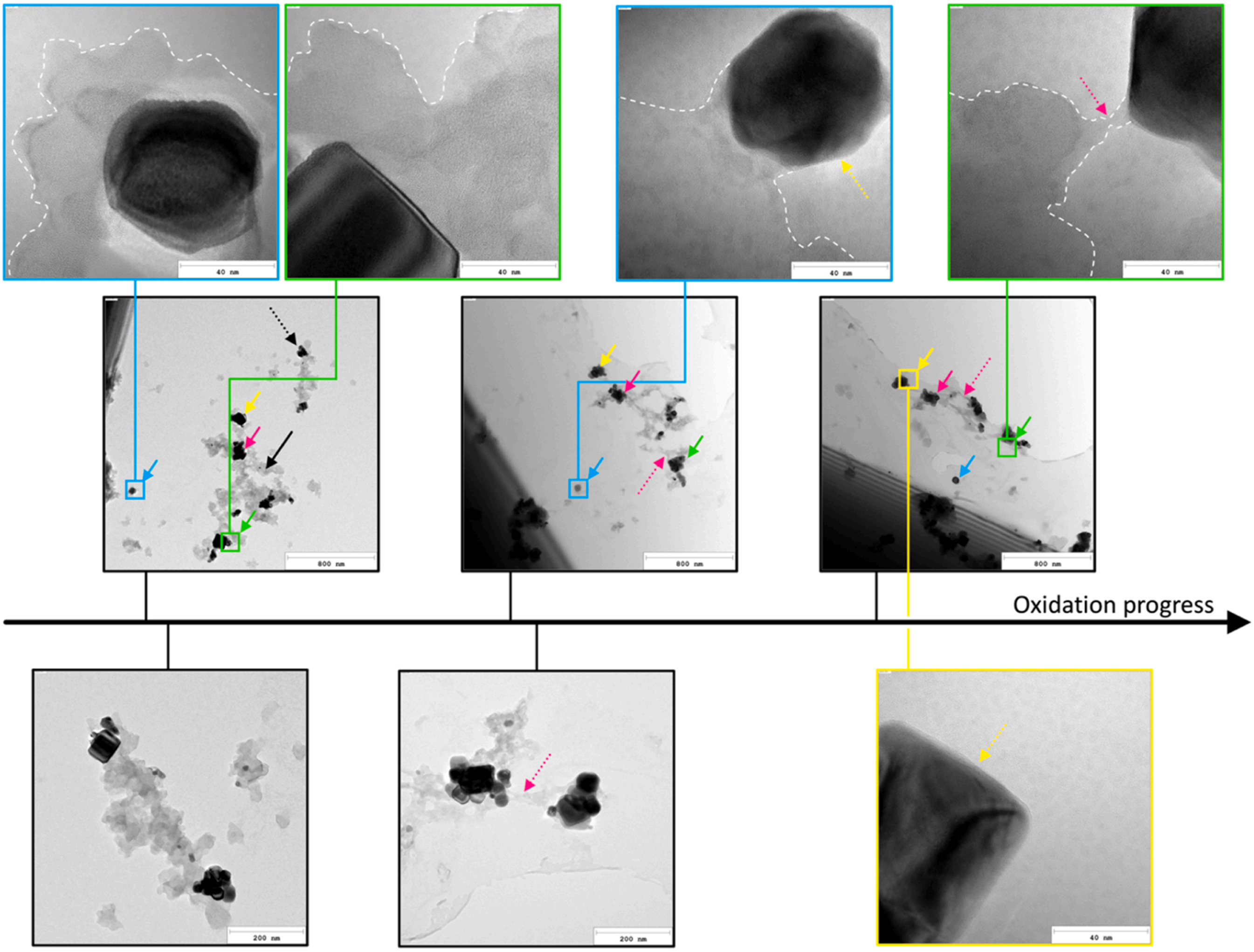

Fig. 9. HRTEM sequence of CeO_2 particles in contact with MFS-C_2H_2 soot during stepwise oxidation. The fresh mixture is shown on the left, while the other two series of images were obtained in the same position after multiple ex-situ oxidation steps in the TGA, each one performed at 575 °C in 10 vol% O_2 in N_2 for 200 s (see Section 2.4). The black dotted arrow pointing to the right marks a catalyst particle, while the black straight arrow pointing to the left highlights the surrounding soot region. Additional colored arrows were included to guide the reader through the oxidation progress across the image sequence. The red dotted arrows indicate temporarily remaining soot bridges, while the yellow dotted arrows highlight newly exposed blank catalyst surfaces after local soot consumption. White dashed contours indicate soot regions throughout the sequence.

associated with the abundance of Lewis acid sites, i.e. electron pair acceptor sites on the catalyst surface. These sites typically correspond to coordinatively unsaturated metal cations, often located near oxygen vacancies. Since they can snatch electrons from carbon atoms at the soot-catalyst interface, these sites facilitate the formation of highly reactive carbocation intermediates [81,101]. These activated species promote the oxidative cracking and progressive decomposition of the graphitic matrix [30], through reaction with surface active oxygen (O_α and O_γ species) or catalyst lattice oxygen (via MvK-like mechanism). Hence, the presence of strong Lewis acid sites ensures that carbon particles are effectively and continuously consumed, preventing the formation of isolated soot aggregates. Overall, all these factors account for the high catalytic activity of Ce50La50 in soot oxidation, making it an effective catalyst even under loose contact conditions.

4. Conclusions

In this work, the effect of soot physicochemical properties on catalytic oxidation was systematically investigated using a set of soot samples with different nanostructure, particle size, and intrinsic reactivity, combined with three ceria-based nanocatalysts. By varying the soot type, the catalyst properties, and the degree of solid-solid contact, a comprehensive view of the factors governing soot oxidation was provided.

Non-catalytic oxidation experiments confirmed that soot reactivity is primarily related to nanostructural order, as reflected by fringe length distribution, C/H ratio, and primary particle size, while the specific surface area plays a minor role. These trends were preserved under catalytic conditions, demonstrating that soot properties remain a dominant factor even in the presence of active catalysts. Among the investigated catalysts, rare earth-doped ceria materials outperformed pure ceria across all soot types and contact modes, following the activity order Ce50La50 > Ce50Pr50 > CeO_2. The enhanced performance of the mixed oxides arises from a synergistic combination of factors, including increased oxygen storage and release capacity, higher abundance of surface oxygen species, and the presence of medium-strength Lewis acid sites, which facilitate interfacial reactions at the soot-catalyst interface.

Stepwise oxidation experiments combined with HRTEM tracking revealed that Ce50La50 uniquely undergoes dynamic restructuring during soot oxidation, forming new contact sites as the reaction progresses. This ability to renew soot-catalyst interfaces explains its superior performance under loose contact conditions, which are

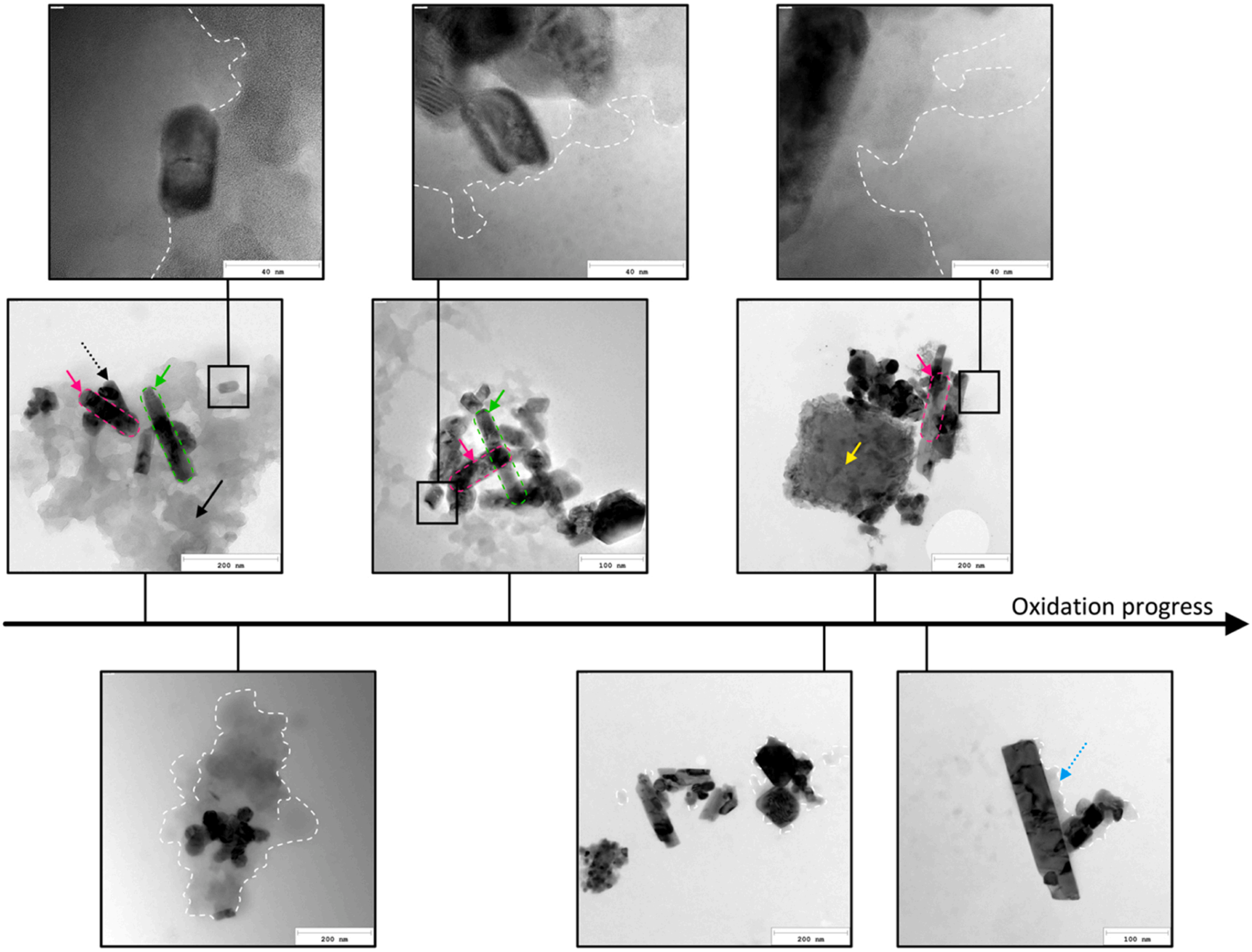

Fig. 10. HRTEM sequence of Ce50La50 nanocubes amidst rod-like structures in contact with MFS-C_2H_2 soot during stepwise oxidation. The fresh mixture is shown on the left, while the other series of images were obtained in the same position after multiple ex-situ oxidation steps in the TGA, each one performed at 575 °C in 10 vol% O_2 in N_2 for 200 s (see Section 2.4). The black dotted arrow pointing to the right marks a catalyst particle, while the black straight arrow pointing to the left highlights the surrounding soot region. Additional colored arrows and contours were included to guide the reader through the oxidation progress across the image sequence. White dashed contours indicate soot regions throughout the sequence.

representative of practical particulate filter operation. However, catalyst restructuring may be accompanied by clustering and surface area loss, leading to a gradual decline in activity upon repeated use.

Overall, the results demonstrate that catalytic soot oxidation is governed by a complex interplay between soot nanostructure, catalyst surface chemistry, and contact dynamics. These findings emphasize the importance of considering soot variability when evaluating catalyst performance and demonstrate that the ability of a catalyst to dynamically create new contact sites with soot during oxidation is crucial, providing useful guidance for the rational design of active soot oxidation catalysts.

CRediT authorship contribution statement

Samir Bensaid: Writing – review & editing, Supervision, Formal analysis, Conceptualization. **Dimosthenis Trimis:** Writing – review & editing, Supervision. **Henning Bockhorn:** Writing – review & editing, Supervision, Formal analysis, Conceptualization. **Marco Piumetti:** Writing – review & editing, Supervision. **Chiara Novara:** Writing – review & editing, Methodology. **Fabian P. Hagen:** Writing – review & editing, Writing – original draft, Investigation, Formal analysis, Data curation, Conceptualization. **Enrico Sartoretti:** Writing – review & editing, Writing – original draft, Investigation, Formal analysis, Data curation, Conceptualization.

Declaration of Competing Interest

The authors declare that they have no known competing financial interests or personal relationships that could have appeared to influence the work reported in this paper.

Acknowledgements

The authors kindly thank Alberto Grosso and Christian Parisella for helping in data collection and catalyst testing during the preparation of their MS thesis, and Camilla Galletti for performing XRD. E.S. acknowledges the PON Ricerca e Innovazione “REACT-EU” project (DM 1062/21). The authors gratefully acknowledge the Research Association for Combustion Engines e.V. (FVV) for financial support within the project FVV1494.

Appendix A. Supporting information

Supplementary data associated with this article can be found in the online version at doi:10.1016/j.jece.2026.123057.

Data availability

Data will be made available on request.

References

[1] S.E. Alexeeff, N.S. Liao, X. Liu, S.K. Van Den Eeden, S. Sidney, Long-term $PM_{2.5}$ exposure and risks of ischemic heart disease and stroke events: review and meta-analysis, J. Am. Heart Assoc. 10 (2021) 1–22, https://doi.org/10.1161/JAHA.120.016890.

[2] V.A. Southerland, M. Brauer, A. Mohegh, M.S. Hammer, A. van Donkelaar, R. V. Martin, J.S. Apte, S.C. Anenberg, Global urban temporal trends in fine particulate matter ($PM_{2.5}$) and attributable health burdens: estimates from global datasets, Lancet Planet. Heal 6 (2022) e139–e146, https://doi.org/10.1016/S2542-5196(21)00350-8.

[3] P.P. Nyayapathi, S. Namuduri, S.K. Kolli, A comprehensive review of vertical profiling of ambient air quality-particulate matter and its impacts on climatic & environmental health, 2025 185, Air Qual. Atmos. Heal 18 (2025) 1569–1595, https://doi.org/10.1007/S11869-025-01697-5.

[4] B. Guan, R. Zhan, H. Lin, Z. Huang, Review of the state-of-the-art of exhaust particulate filter technology in internal combustion engines, J. Environ. Manag. 154 (2015) 225–258, https://doi.org/10.1016/j.jenvman.2015.02.027.

[5] R. Matarrese, Catalytic materials for gasoline particulate filters soot oxidation, Catalysts 11 (2021) 1–21, https://doi.org/10.3390/catal11080890.

[6] J. Luo, H. Zhang, X. Chen, L. Ye, M. Li, Y. Tie, S. Xu, G. Chen, C. Jiang, The evaluation of catalytic activity, reaction mechanism and catalyst classification in diesel particulate filter: a review, Clean. Technol. Environ. Policy 26 (2024) 3183–3225, https://doi.org/10.1007/s10098-024-02819-w.

[7] T. Zhao, Z. Song, C. Wu, Y. Li, H. Li, Y. Wei, S. Yao, M. Xiao, M. Zhao, B. Cui, Advancements in cobalt-based oxide catalysts for soot oxidation: enhancing catalytic performance through modification and morphology control, Smart Mol. 2 (2024) e20240024, https://doi.org/10.1002/SMO.20240024.

[8] M. Piumetti, B. van der Linden, M. Makkee, P. Miceli, D. Fino, N. Russo, S. Bensaid, Contact dynamics for a solid-solid reaction mediated by gas-phase oxygen: Study on the soot oxidation over ceria-based catalysts, Appl. Catal. B Environ. 199 (2016) 96–107, https://doi.org/10.1016/j.apcatb.2016.06.006.

[9] L. Lisi, G. Landi, V. Di Sarli, The Issue of Soot-Catalyst Contact in Regeneration of Catalytic Diesel Particulate Filters: A Critical Review, 2020, Vol. 10, Page 1307, Catal 10 (2020) 1307, https://doi.org/10.3390/CATAL10111307.

[10] F. Martinovic, C. Galletti, S. Bensaid, R. Pirone, F.A. Deorsola, Soot oxidation in low-O2 and O2-free environments by lanthanum-based perovskites: structural changes and the effect of Ag doping, Catal. Sci. Technol. 12 (2022) 5453–5464, https://doi.org/10.1039/d2cy00841f.

[11] V. Alcalde-Santiago, A. Davó-Quiñonero, D. Lozano-Castelló, A. Bueno-López, On the soot combustion mechanism using 3DOM ceria catalysts, Appl. Catal. B Environ. 234 (2018) 187–197, https://doi.org/10.1016/j.apcatb.2018.04.023.

[12] C. Zhang, D. Yu, C. Peng, L. Wang, X. Yu, Y. Wei, J. Liu, Z. Zhao, Research progress on preparation of 3DOM-based oxide catalysts and their catalytic performances for the combustion of diesel soot particles, Appl. Catal. B Environ. 319 (2022), https://doi.org/10.1016/j.apcatb.2022.121946.

[13] S. Yang, J. Wang, W. Chai, J. Zhu, Y. Men, Enhanced soot oxidation activity over CuO/CeO2 mesoporous nanosheets, Catal. Sci. Technol. 9 (2019) 1699–1709, https://doi.org/10.1039/C8CY02605J.

[14] Y.C. Tsai, M.C. Wan, S.Y. Lin, V.T. Thanh Thuy, N.N. Huy, D.D. Tuan, J. Lee, K.Y. A. Lin, Boosted catalytic soot oxidation by hierarchical hollow cobalt oxide constructed from a Template-Sacrificial Method: Promoting Roles of morphologies and oxygen vacancies, Chem. Eng. J. 510 (2025) 161458, https://doi.org/10.1016/J.CEJ.2025.161458.

[15] P. Miceli, S. Bensaid, N. Russo, D. Fino, Effect of the morphological and surface properties of CeO_2-based catalysts on the soot oxidation activity, Chem. Eng. J. 278 (2015) 190–198, https://doi.org/10.1016/j.cej.2014.10.055.

[16] H. Liang, B. Jin, M. Li, X. Yuan, J. Wan, W. Liu, X. Wu, S. Liu, Highly reactive and thermally stable Ag/YSZ catalysts with macroporous fiber-like morphology for soot combustion, Appl. Catal. B Environ. 294 (2021) 120271, https://doi.org/10.1016/J.APCATB.2021.120271.

[17] P. Legutko, P. Stelmachowski, X. Yu, Z. Zhao, Z. Sojka, A. Kotarba, Catalytic Soot Combustion—General Concepts and Alkali Promotion, ACS Catal. 13 (2023) 3395–3418, https://doi.org/10.1021/acscatal.2c05994.

[18] E. Aneggi, C. de Leitenburg, G. Dolcetti, A. Trovarelli, Diesel soot combustion activity of ceria promoted with alkali metals, Catal. Today 136 (2008) 3–10, https://doi.org/10.1016/j.cattod.2008.01.002.

[19] X. Mei, X. Zhu, Y. Zhang, Z. Zhang, Z. Zhong, Y. Xin, J. Zhang, Decreasing the catalytic ignition temperature of diesel soot using electrified conductive oxide catalysts, Nat. Catal. 4 (2021) 1002–1011, https://doi.org/10.1038/s41929-021-00702-1.

[20] R. Weng, X. Mei, Z. Zhang, Y. Xin, J. Xu, Y. Zhang, J. Zhang, Affecting factors of electrified soot combustion on potassium-supported antimony tin oxides, Chem. Eng. J. 465 (2023) 143046, https://doi.org/10.1016/j.cej.2023.143046.

[21] Z. Tu, G. Wu, C. Zheng, X. Wu, J. Wan, S. Liu, Perspective about gasoline soot combustion over ceria catalysts: A close look into the "active oxygen" enigma, J. Rare Earths 43 (2025) 641–659, https://doi.org/10.1016/j.jre.2024.08.017.

[22] X. Garcia, L. Soler, A. Casanovas, C. Escudero, J. Llorca, X-ray photoelectron and Raman spectroscopy of nanostructured ceria in soot oxidation under operando conditions, Carbon N. Y. 178 (2021) 164–180, https://doi.org/10.1016/j.carbon.2021.03.009.

[23] S. Zhang, P. Wang, Z. Xu, M. Gong, J. Cao, J. Shen, X. Fang, X. Xu, J. Xu, X. Wang, Insights into the exceptional support phase effect on $Ag/Sm_2Ce_2O_7$: Modulating Ag distribution and Ag-support interaction to construct reactive soot oxidation catalysts, J. Catal. 442 (2025), https://doi.org/10.1016/j.jcat.2024.115893.

[24] J.C. Martínez-Munuera, M. Zoccoli, J. Giménez-Mañogil, A. García-García, Lattice oxygen activity in ceria-praseodymia mixed oxides for soot oxidation in catalysed Gasoline Particle Filters, Appl. Catal. B Environ. 245 (2019) 706–720, https://doi.org/10.1016/j.apcatb.2018.12.076.

[25] X. Mao, S. Liu, W. Liu, X. Wu, S. Liu, A simple model catalyst study to distinguish the roles of different oxygen species in propane and soot combustion, Appl. Catal. B Environ. 310 (2022) 121331, https://doi.org/10.1016/J.APCATB.2022.121331.

[26] C. Wang, H. Yuan, G. Lu, H. Wang, Oxygen vacancies and alkaline metal boost CeO_2 catalyst for enhanced soot combustion activity: A first-principles evidence, Appl. Catal. B Environ. 281 (2021) 119468, https://doi.org/10.1016/J.APCATB.2020.119468.

[27] Y. Li, T. Qin, L. Xu, Y. Ma, H. Guo, J. Xiong, P. Zhang, Z. Zhao, X. Liu, Y. Liu, J. Zou, L. Chen, Y. Wei, Enhancing Catalytic Removal of Autoexhaust Soot Particles via the Modulation of Interfacial Oxygen Vacancies in Cu/CeO_2 Catalysts, Environ. Sci. Technol. (2025), https://doi.org/10.1021/acs.est.4c12325.

[28] L. Castoldi, E. Aneggi, R. Matarrese, R. Bonzi, J. Llorca, A. Trovarelli, L. Lietti, Silver-based catalytic materials for the simultaneous removal of soot and NO_x, Catal. Today 258 (2015) 405–415, https://doi.org/10.1016/j.cattod.2015.02.024.

[29] M.V. Grabchenko, G.V. Mamontov, V.I. Zaikovskii, V. La Parola, L.F. Liotta, O. V. Vodyankina, The role of metal–support interaction in Ag/CeO_2 catalysts for CO and soot oxidation, Appl. Catal. B Environ. 260 (2020) 118148, https://doi.org/10.1016/j.apcatb.2019.118148.

[30] S. Liu, X. Wu, S. Liu, R. Ran, D. Weng, Acid modification of platinum-based soot oxidation catalysts: A short review, J. Ind. Eng. Chem. 142 (2025) 34–44, https://doi.org/10.1016/j.jiec.2024.07.029.

[31] P. Yao, Y. Huang, Y. Jiao, H. Xu, J. Wang, Y. Chen, Soot oxidation over Pt-loaded CeO_2-ZrO_2 catalysts under gasoline exhaust conditions: Soot-catalyst contact efficiency and Pt chemical state, Fuel 334 (2023) 126782, https://doi.org/10.1016/j.fuel.2022.126782.

[32] A.A. Khaskheli, L. Xu, D. Liu, Manganese Oxide-Based Catalysts for Soot Oxidation: A Review on the Recent Advances and Future Directions, Energy Fuels 36 (2022) 7362–7381, https://doi.org/10.1021/acs.energyfuels.2c01492.

[33] R. Nithya, A.L. Vikram, H. Dasari, S. Nethaji, Enhanced Catalytic Efficiency of CuMn2O4 in Soot Oxidation: An Investigation into Its Synthesis and Characterization, Catal. Lett. 155 (2025) 1–8, https://doi.org/10.1007/S10562-025-04955-4.

[34] S. Bensaid, N. Russo, Low temperature DPF regeneration by delafossite catalysts, Catal. Today 176 (2011) 417–423, https://doi.org/10.1016/j.cattod.2010.11.020.

[35] D. Reichert, H. Bockhorn, S. Kureti, Study of the reaction of NO_x and soot on Fe_2O_3 catalyst in excess of O_2, Appl. Catal. B Environ. 80 (2008) 248–259, https://doi.org/10.1016/j.apcatb.2007.11.024.

[36] S. Liu, X. Wu, D. Weng, R. Ran, Ceria-based catalysts for soot oxidation: A review, J. Rare Earths 33 (2015) 567–590, https://doi.org/10.1016/S1002-0721(14)60457-9.

[37] N. Guillén-Hurtado, J. Giménez-Mañogil, J.C. Martínez-Munuera, A. Bueno-López, A. García-García, Study of Ce/Pr ratio in ceria-praseodymia catalysts for soot combustion under different atmospheres, Appl. Catal. A Gen. 590 (2020) 117339, https://doi.org/10.1016/j.apcata.2019.117339.

[38] E. Sartoretti, C. Novara, A. Chiodoni, F. Giorgis, M. Piumetti, S. Bensaid, N. Russo, D. Fino, Nanostructured ceria-based catalysts doped with La and Nd: How acid-base sites and redox properties determine the oxidation mechanisms, Catal. Today 390–391 (2022) 117–134, https://doi.org/10.1016/J.CATTOD.2021.11.040.

[39] A. García-Cuenca, I. Mekki, A. García-García, Effect of copper and manganese as active phases in ceria and ceria-praseodymia catalysts for soot combustion in the exhaust of Gasoline Direct Injection (GDI) vehicles, Appl. Catal. B Environ. 370 (2025) 125180, https://doi.org/10.1016/j.apcatb.2025.125180.

[40] D. Yu, Y. Ren, Y. Zhang, S. Gao, X. Zhang, X. Chen, S. Chen, L. Wang, C. Zhang, X. Yu, X. Fan, Z. Zhao, Investigation of sodium–manganese oxides with various crystal phases for the efficient catalytic removal of diesel soot particles, Appl. Catal. B Environ. 358 (2024), https://doi.org/10.1016/j.apcatb.2024.124407.

[41] A. Bueno-López, Diesel soot combustion ceria catalysts, Appl. Catal. B Environ. 146 (2014) 1–11, https://doi.org/10.1016/j.apcatb.2013.02.033.

[42] P. Woźniak, Ce(III) formate-derived hierarchical cerium oxide particles with icosahedral symmetry-based architectures: Effect of third level of structural hierarchy in soot and propane oxidation, Acta Mater. 281 (2024), https://doi.org/10.1016/j.actamat.2024.120372.

[43] S.B. Putla, M. Kamali, B. Swapna, B.M. Reddy, P. Sudarsanam, Review of Shape-Controlled CeO_2 Nanocatalysts for Purification of Auto-Exhaust Pollutants, ACS Appl. Nano Mater. 7 (2024) 6749–6771, https://doi.org/10.1021/ACSANM.4C00228.

[44] M. Gao, Y. Jang, L. Ding, Y. Gao, S. Dai, Z. Dai, G. Yu, W. Yang, F. Wang, Mechanism of the noncatalytic oxidation of soot using in situ transmission

electron microscopy, Nat. Commun. 14 (2023) 1–12, https://doi.org/10.1038/s41467-023-41726-4.

[45] F.P. Hagen, A. Rinkenburger, J. Günther, H. Bockhorn, R. Niessner, R. Suntz, A. Loukou, D. Trimis, C. Haisch, Spark discharge-generated soot: Varying nanostructure and reactivity against oxidation with molecular oxygen by synthesis conditions, J. Aerosol Sci. 143 (2020) 105530, https://doi.org/10.1016/j.jaerosci.2020.105530.

[46] F. Hagen, F. Hardock, S. Koch, N. Sebbar, H. Bockhorn, A. Loukou, H. Kubach, R. Suntz, D. Trimis, T. Koch, Why Soot is not Alike Soot: A Molecular/Nanostructural Approach to Low Temperature Soot Oxidation, Flow. Turbul. Combust. 106 (2021) 295–329, https://doi.org/10.1007/s10494-020-00205-2.

[47] F.P. Hagen, D. Kretzler, T. Häber, H. Bockhorn, R. Suntz, D. Trimis, Carbon nanostructure and reactivity of soot particles from non-intrusive methods based on UV–VIS spectroscopy and time-resolved laser-induced incandescence, Carbon N. Y. 182 (2021) 634–654, https://doi.org/10.1016/j.carbon.2021.06.006.

[48] J. Huang, J. Gao, J. Liu, X. Wang, G. Tian, H. Chen, A Review of the Application of Soot Catalysts: Focus on the Soot Oxidation-Induced Fragmentation Process, Energy Fuels 38 (2024) 20057–20083, https://doi.org/10.1021/acs.energyfuels.4c03152.

[49] J. Gao, Y. Wang, S. Wang, X. Li, X. Chang, X. Wang, C. Yang, R. Xuan, Effect of catalytic reactions on soot feature evolutions in oxidation process, Chem. Eng. J. 443 (2022) 136392, https://doi.org/10.1016/j.cej.2022.136392.

[50] J. Huang, S. Wang, X. Wang, J. Gao, Y. Wang, G. Tian, Study on the differences between non-catalytic and catalytic oxidation of soot based on catalyst CeO2, J. Energy Inst. 113 (2024) 101506, https://doi.org/10.1016/j.joei.2023.101506.

[51] J. Wei, C. Fan, Y. Zhuang, Z. Fu, Z. Guan, H. Li, D. Li, Y. Qian, Diesel soot combustion over ceria catalyst: Evolution of functional groups on soot surfaces, Fuel 338 (2023) 127391, https://doi.org/10.1016/j.fuel.2023.127391.

[52] V. Di Sarli, G. Landi, L. Lisi, A. Saliva, A. Di Benedetto, Catalytic diesel particulate filters with highly dispersed ceria: Effect of the soot-catalyst contact on the regeneration performance, Appl. Catal. B Environ. 197 (2016) 116–124, https://doi.org/10.1016/j.apcatb.2016.01.073.

[53] K. Krishna, A. Bueno-López, M. Makkee, J.A. Moulijn, Potential rare-earth modified CeO$_2$ catalysts for soot oxidation. Part III. Effect of dopant loading and calcination temperature on catalytic activity with O$_2$ and NO + O$_2$, Appl. Catal. B Environ. 75 (2007) 210–220, https://doi.org/10.1016/j.apcatb.2007.04.009.

[54] T. Andana, M. Piumetti, S. Bensaid, N. Russo, D. Fino, R. Pirone, Nanostructured ceria-praseodymia catalysts for diesel soot combustion, Appl. Catal. B Environ. 197 (2016) 125–137, https://doi.org/10.1016/j.apcatb.2015.12.030.

[55] T. Andana, M. Piumetti, S. Bensaid, N. Russo, D. Fino, Heterogeneous mechanism of NOx-assisted soot oxidation in the passive regeneration of a bench-scale diesel particulate filter catalyzed with nanostructured equimolar ceria-praseodymia, Appl. Catal. A Gen. 583 (2019) 117136, https://doi.org/10.1016/j.apcata.2019.117136.

[56] E. Sartoretti, F. Martini, M. Piumetti, S. Bensaid, N. Russo, D. Fino, Nanostructured Equimolar Ceria-Praseodymia for Total Oxidations in Low-O$_2$ Conditions, Catalysts 10 (2020) 1–16, https://doi.org/10.3390/catal10020165.

[57] L. Katta, P. Sudarsanam, G. Thrimurthulu, B.M. Reddy, Doped nanosized ceria solid solutions for low temperature soot oxidation: Zirconium versus lanthanum promoters, Appl. Catal. B Environ. 101 (2010) 101–108, https://doi.org/10.1016/j.apcatb.2010.09.012.

[58] E. Sartoretti, C. Novara, M. Fontana, F. Giorgis, M. Piumetti, S. Bensaid, N. Russo, D. Fino, New insights on the defect sites evolution during CO oxidation over doped ceria nanocatalysts probed by in situ Raman spectroscopy, Appl. Catal. A Gen. 596 (2020) 117517, https://doi.org/10.1016/j.apcata.2020.117517.

[59] F.P. Hagen, H. Bockhorn, H. Störmer, A. Loukou, R. Suntz, D. Trimis, Nanostructural and morphological characteristics of single soot aggregates during low-temperature oxidation, Proc. Combust. Inst. 38 (2021) 1153–1161, https://doi.org/10.1016/J.PROCI.2020.06.338.

[60] P. Vinchhi, A. Ray, K. Mallik, R. Pati, Gd-doped ceria with extraordinary oxygen-ion conductivity for low temperature solid oxide fuel cells, Sci. Rep. 14 (2024) 1–13, https://doi.org/10.1038/s41598-024-59030-6.

[61] M. Arduino, E. Sartoretti, E. Calì, S. Bensaid, F.A. Deorsola, Understanding the Role of Morphology in the Direct Synthesis of Diethyl Carbonate Over Ceria-Based Catalysts: An In Situ Infrared and High-Resolution TEM Study, ChemCatChem 17 (2025), https://doi.org/10.1002/cctc.202500140.

[62] M.M. Ravindra, R. Shirasangi, H.P. Dasari, M.B. Saidutta, Fabrication of praseodymium-doped ceria (PDC) films by slurry spin-coating technique and its structural, morphological and optical properties, Appl. Surf. Sci. Adv. 16 (2023) 100413, https://doi.org/10.1016/j.apsadv.2023.100413.

[63] S. Ballauri, E. Sartoretti, M. Castellino, M. Armandi, M. Piumetti, D. Fino, N. Russo, S. Bensaid, Mesoporous Ceria and Ceria-Praseodymia as High Surface Area Supports for Pd-based Catalysts with Enhanced Methane Oxidation Activity, ChemCatChem 16 (2024) e202301359, https://doi.org/10.1002/cctc.202301359.

[64] S. Loridant, Raman spectroscopy as a powerful tool to characterize ceria-based catalysts, Catal. Today (2020) 1–14, https://doi.org/10.1016/j.cattod.2020.03.044.

[65] M. Dosa, M.J. Marin Figueredo, E. Sartoretti, C. Novara, F. Giorgis, S. Bensaid, D. Fino, N. Russo, M. Piumetti, Cerium-Copper Oxides Synthesized in a Multi-Inlet Vortex Reactor as Effective Nanocatalysts for CO and Ethene Oxidation Reactions, Catalysts 12 (2022) 1–23, https://doi.org/10.3390/catal12040364.

[66] Z. Zhao, G. Gao, Y. Xi, J. Wang, P. Sun, Q. Liu, C. Li, Z. Huang, F. Li, Inverse ceria-nickel catalyst for enhanced C – O bond hydrogenolysis of biomass and polyether, Nat. Commun. 15 (2024) 8444, https://doi.org/10.1038/s41467-024-52704-9.

[67] S. Ballauri, E. Sartoretti, C. Novara, F. Giorgis, M. Piumetti, D. Fino, N. Russo, S. Bensaid, Wide range temperature stability of palladium on ceria-praseodymia catalysts for complete methane oxidation, Catal. Today 390–391 (2022) 185–197, https://doi.org/10.1016/j.cattod.2021.11.035.

[68] A. Westermann, C. Geantet, P. Vernoux, S. Loridant, Defects band enhanced by resonance Raman effect in praseodymium doped CeO$_2$, J. Raman Spectrosc. 47 (2016) 1276–1279, https://doi.org/10.1002/jrs.4943.

[69] L. Chen, P. Fleming, V. Morris, J.D. Holmes, M.A. Morris, Size-Related Lattice Parameter Changes and Surface Defects in Ceria Nanocrystals, J. Phys. Chem. C. 114 (2010) 12909–12919, https://doi.org/10.1021/jp1031465.

[70] Z. Wu, A.K.P. Mann, M. Li, S.H. Overbury, Spectroscopic investigation of surface dependent acid base property of ceria nanoshapes, J. Phys. Chem. C. 119 (2015) 7340–7350, https://doi.org/10.1021/acs.jpcc.5b00859.

[71] X. Yao, L. Chen, T. Kong, S. Ding, Q. Luo, F. Yang, Support effect of the supported ceria-based catalysts during NH$_3$-SCR reaction, Chin. J. Catal. 38 (2017) 1423–1430, https://doi.org/10.1016/S1872-2067(17)62868-7.

[72] E. Corrao, F. Salomone, E. Giglio, M. Castellino, S.M. Ronchetti, M. Armandi, R. Pirone, S. Bensaid, CO$_2$ conversion into hydrocarbons via modified Fischer-Tropsch synthesis by using bulk iron catalysts combined with zeolites, Chem. Eng. Res. Des. 197 (2023) 449–465, https://doi.org/10.1016/J.CHERD.2023.07.052.

[73] B. Zhang, S. Zhang, B. Liu, Effect of oxygen vacancies on ceria catalyst for selective catalytic reduction of NO with NH$_3$, Appl. Surf. Sci. 529 (2020) 147068, https://doi.org/10.1016/j.apsusc.2020.147068.

[74] C. Cocuzza, E. Sartoretti, C. Novara, F. Giorgis, S. Bensaid, N. Russo, D. Fino, M. Piumetti, Copper-manganese oxide catalysts prepared by solution combustion synthesis for total oxidation of VOCs, Catal. Today 423 (2023) 114292, https://doi.org/10.1016/j.cattod.2023.114292.

[75] C. Tang, H. Zhang, L. Dong, Ceria-based catalysts for low-temperature selective catalytic reduction of NO with NH3, Catal. Sci. Technol. 6 (2016) 1248–1264, https://doi.org/10.1039/c5cy01487e.

[76] M. Li, J. Zhang, S.C. Purdy, F. Lin, K.A. Unocic, M. Cordon, Z. Wu, H. Wang, J. Hall, A.J. Kropf, T.R. Krause, B. Davison, Z. Li, A.D. Sutton, Tailoring olefin distribution via tuning rare earth metals in bifunctional Cu-RE/beta-zeolite catalysts for ethanol upgrading, Appl. Catal. B Environ. 344 (2024) 123648, https://doi.org/10.1016/j.apcatb.2023.123648.

[77] D.M. Sung, Y.H. Kim, E.D. Park, J.E. Yie, Correlation between acidity and catalytic activity for the methanol dehydration over various aluminum oxides, 2010 366, Res. Chem. Inter. 36 (2010) 653–660, https://doi.org/10.1007/S11164-010-0201-Y.

[78] H. Pérez-Pastenes, A. Ochoa-Tapia, T. Viveros, A. Montoya, Influence of the synthesis method on the properties of ceria-doped alumina, J. Sol. Gel Sci. Technol. 37 (2006) 49–56, https://doi.org/10.1007/s10971-005-5063-1.

[79] F. Salomone, G. Ferrarelli, E. Giglio, E. Corrao, M. Migliori, S. Bensaid, R. Pirone, G. Giordano, Hierarchical zeolites for dimethyl ether dehydration into light olefins, Catal. Today 463 (2026), https://doi.org/10.1016/j.cattod.2025.115618.

[80] S. Liu, X. Wu, H. Luo, D. Weng, R. Ran, Pt/zeolite catalysts for soot oxidation: influence of hydrothermal aging, J. Phys. Chem. C. 119 (2015) 17218–17227, https://doi.org/10.1021/acs.jpcc.5b04882.

[81] S. Liu, X. Wu, D. Weng, M. Li, R. Ran, Roles of acid sites on Pt/H-ZSM5 catalyst in catalytic oxidation of diesel soot, ACS Catal. 5 (2015) 909–919, https://doi.org/10.1021/cs5018369.

[82] B. Azambre, L. Zenboury, J.V. Weber, P. Burg, Surface characterization of acidic ceria-zirconia prepared by direct sulfation, Appl. Surf. Sci. 256 (2010) 4570–4581, https://doi.org/10.1016/j.apsusc.2010.02.049.

[83] N. Azaria, D. Schweke, L. Shelly, S. Hayun, Effect of La addition to ceria on the oxygen storage capacity and the energetics of water adsorption, Chem. Mater. (2024), https://doi.org/10.1021/ACS.CHEMMATER.4C02109.

[84] M. Gajendiran, J. Ota, V. Pandey, R. Bagai, S.K. Hait, C. Kannan, S.S. V. Ramakumar, Surface oxygen vacancy vs oxygen storage capacity in cubic ceria based nanocatalysts for low temperature catalytic combustion of fuels, J. Ind. Eng. Chem. 139 (2024) 434–443, https://doi.org/10.1016/J.JIEC.2024.05.018.

[85] N. Grifasi, E. Sartoretti, P. Legutko, S. Bensaid, N. Russo, A. Adamski, D. Fino, M. Piumetti, Copper-manganese oxide catalysts for low-temperature oxidation of indoor pollutants, Appl. Catal. B Environ. 385 (2026) 126292, https://doi.org/10.1016/j.apcatb.2025.126292.

[86] H. Zhang, S. Sui, X. Zheng, R. Cao, P. Zhang, One-pot synthesis of atomically dispersed Pt on MnO$_2$ for efficient catalytic decomposition of toluene at low temperatures, Appl. Catal. B Environ. 257 (2019) 117878, https://doi.org/10.1016/J.APCATB.2019.117878.

[87] T. Andana, M. Piumetti, S. Bensaid, N. Russo, D. Fino, R. Pirone, CO and soot oxidation over Ce-Zr-Pr oxide catalysts, Nanoscale Res. Lett. 11 (2016) 1–9, https://doi.org/10.1186/s11671-016-1494-6.

[88] D. Mukherjee, B.G. Rao, B.M. Reddy, CO and soot oxidation activity of doped ceria: Influence of dopants, Appl. Catal. B Environ. 197 (2016) 105–115, https://doi.org/10.1016/j.apcatb.2016.03.042.

[89] P. Yao, J. He, X. Jiang, Y. Jiao, J. Wang, Y. Chen, Factors determining gasoline soot abatement over CeO$_2$–ZrO$_2$-MnO$_x$ catalysts under low oxygen concentration condition, J. Energy Inst. 93 (2020) 774–783, https://doi.org/10.1016/j.joei.2019.05.005.

[90] M. Lykaki, E. Pachatouridou, S.A.C. Carabineiro, E. Iliopoulou, C. Andriopoulou, N. Kallithrakas-Kontos, S. Boghosian, M. Konsolakis, Ceria nanoparticles shape effects on the structural defects and surface chemistry: Implications in CO oxidation by Cu/CeO$_2$ catalysts, Appl. Catal. B Environ. 230 (2018) 18–28, https://doi.org/10.1016/j.apcatb.2018.02.035.

[91] N. Grifasi, E. Sartoretti, D. Montesi, S. Bensaid, N. Russo, F. Deorsola, D. Fino, C. Novara, F. Giorgis, M. Piumetti, Mesostructured manganese oxides for efficient

catalytic oxidation of CO, ethylene, and propylene at mild temperatures: insight into the role of crystalline phases and physico-chemical properties, Appl. Catal. B Environ. Energy 362 (2025) 124696, https://doi.org/10.1016/j.apcatb.2024.124696.

[92] S.S. Patil, H.P. Dasari, R. Shirasangi, H. Dasari, Diesel soot oxidation over Mn–Pr–Ce oxide catalysts: structural changes and the impact of Mn doping, Mater. Adv. 6 (2025) 1131–1143, https://doi.org/10.1039/d4ma00968a.

[93] D.J. Morgan, Photoelectron spectroscopy of ceria: Reduction, quantification and the myth of the vacancy peak in XPS analysis, Surf. Interface Anal. 55 (2023) 845–850, https://doi.org/10.1002/sia.7254.

[94] K. Polychronopoulou, A.F. Zedan, M. AlKetbi, S. Stephen, M. Ather, M. S. Katsiotis, J. Arvanitidis, D. Christofilos, A.F. Isakovic, S. AlHassan, Tailoring the efficiency of an active catalyst for CO abatement through oxidation reaction: the case study of samarium-doped ceria, J. Environ. Chem. Eng. 6 (2018) 266–280, https://doi.org/10.1016/j.jece.2017.12.001.

[95] G. Pampararo, E. Sartoretti, A.S. Traoré, O. Ersen, C. Novara, S. Bensaid, D. P. Debecker, Spray-made porous CuO-CeO_2 microspheres rival precious metal catalysts for the low-temperature oxidation of air pollutants, J. Environ. Chem. Eng. 13 (2025) 116753, https://doi.org/10.1016/j.jece.2025.116753.

[96] E. Poggio-Fraccari, G. Baronetti, F. Mariño, Pr^{3+} surface fraction in CePr mixed oxides determined by XPS analysis, J. Electron Spectros. Relat. Phenom. 222 (2018) 1–4, https://doi.org/10.1016/j.elspec.2017.11.003.

[97] M. Uma, N. Balaram, P.R. Sekhar Reddy, V. Janardhanam, V. Rajagopal Reddy, H. J. Yun, S.N. Lee, C.J. Choi, Structural, chemical and electrical properties of Au/La_2O_3/n-GaN MIS junction with a High-k lanthanum oxide insulating layer, J. Electron. Mater. 48 (2019) 4217–4225, https://doi.org/10.1007/s11664-019-07193-8.

[98] G. Gao, L. Yang, B. Dai, F. Xia, Z. Yang, S. Guo, P. Wang, F. Geng, J. Han, J. Zhu, Investigation of the effect of annealing temperature on optical properties of lanthanum-oxide thin films prepared by sol-gel method, Surf. Coat. Technol. 365 (2019) 164–172, https://doi.org/10.1016/j.surfcoat.2018.07.001.

[99] J.O. Müller, D.S. Su, U. Wild, R. Schlögl, Bulk and surface structural investigations of diesel engine soot and carbon black, Phys. Chem. Chem. Phys. 9 (2007) 4018–4025, https://doi.org/10.1039/B704850E.

[100] C. Lee, Y. Jeon, S. Hata, J.Il Park, R. Akiyoshi, H. Saito, Y. Teraoka, Y.G. Shul, H. Einaga, Three-dimensional arrangements of perovskite-type oxide nano-fiber webs for effective soot oxidation, Appl. Catal. B Environ. 191 (2016) 157–164, https://doi.org/10.1016/J.APCATB.2016.03.001.

[101] P. Sudarsanam, B. Hillary, M.H. Amin, N. Rockstroh, U. Bentrup, A. Brückner, S. K. Bhargava, Heterostructured copper-ceria and iron-ceria nanorods: role of morphology, redox, and acid properties in catalytic diesel soot combustion, Langmuir 34 (2018) 2663–2673, https://doi.org/10.1021/acs.langmuir.7b03998.

[102] K. Kim, J.Do Yoo, S. Lee, M. Bae, J. Bae, W.C. Jung, J.W. Han, A simple descriptor to rapidly screen CO oxidation activity on rare-earth metal-doped CeO_2: from experiment to first-principles, ACS Appl. Mater. Interfaces 9 (2017) 15449–15458, https://doi.org/10.1021/acsami.7b01844.